International Journal of Naval Architecture and Ocean Engineering 16 (2024) 100606

Contents lists available at ScienceDirect

International Journal of Naval Architecture and Ocean Engineering

journal homepage: www.journals.elsevier.com/international-journal-of-naval-architecture-and-ocean-engineering/

Developing a numerical framework to study the cavitation and non-cavitation behaviour of a centrifugal pump inducer

Seyed Ehsan Hosseini [a], Amin Deyranlou [b], Pouyan Talebizadehsardari [c,*], Hayder I. Mohammed [d], Amir Keshmiri [e,**]

[a] School of Mechanical Engineering, Iran University of Science and Technology, Tehran, Iran
[b] School of Engineering and Computing, University of Central Lancashire, Preston, United Kingdom
[c] Power Electronics, Machines and Control (PEMC) Research Group, University of Nottingham, Nottingham, United Kingdom
[d] Department of Cooling And Air Conditioning Engineering, Imam Ja'afar Al-Sadiq University, Baghdad, Iraq
[e] ManchesterCFD team, School of Engineering, The University of Manchester, Manchester, United Kingdom

ARTICLE INFO

Keywords:
Axial inducer
Computational fluid dynamics
Centrifugal pump
Cavitation
Tip clearance

ABSTRACT

The present work explores the impact of tip clearance on the mean blade height ratio, inlet tip blade angle, and surface roughness of the inducer. The objective is to find an optimized inducer to limit the secondary flow over the blades, which in turn improves the pump efficiency and reduces the life cycle costs. A numerical framework is developed to investigate efficient operational and geometrical parameters on an inducer's cavitation and non-cavitation presentations. The catalyser functioning is simulated by applying a 3D CFD model, and the results are assessed against empirical data. The results show a reliable agreement with empirical data and suggest that the increment of tip clearance in the mean blade height ratio causes the hydraulic performance and the analytical cavitation number to decline in cavitation and non-cavitation conditions. Moreover, the optimum value of 85° is found for the inlet tip blade angle, which improves the non-cavitation performance.

Nomenclature

$\overline{u_i' u_j}$	Reynolds stress tensor
u'	Fluctuating velocity (m/s)
U_j	Mean velocity (m/s)
P	Pressure (Pa)
ΔP	Pressure drop (Pa)
ΔP_t	Total pressure drop (Pa)
Re	Reynolds number $Re = 2\Omega r_T^2/\nu$
k	Turbulent kinetic energy (m^2/s^2)
k_s	Surface roughness (μm)
Ω	Inducer rotational speed (rev/min)
μ	Dynamic viscosity (Pa s)
ρ	Density (kg/m^3)
η	Hydraulic efficiency
τ	Torque (N-m)
δ_{ij}	Kronecker delta
μ_t	Turbulent viscosity (Pa s)
γ	Inlet tip blade angle (deg)
Q	Volumetric flow rate (m^3/s)

(*continued on next column*)

(*continued*)

r_h	Inducer hub radius (m)
r_T	Inducer blade tip radius (m)
r_g	Volume fraction
C_μ	RNG k-ε turbulence model constant (=0.09)
$C_{\varepsilon 1}$	RNG k-ε turbulence model constant (=1.42)
$C_{\varepsilon 2}$	RNG k-ε turbulence model constant (=1.68)
c	Tip clearance to mean blade height ratio
G_k	Turbulent kinetic energy generation ($kg/m\ s^3$)
σ_k	Effective Prandtl number for k
σ_ε	Effective Prandtl number for ε
σ_t	Surface tension coefficient
ϕ	Flow coefficient
ψ	Head coefficient
η_o	Constant (=4.38)
ε	Rate of dissipation of turbulent kinetic energy (m^2/s^3)
γ	Inlet tip blade angle (deg)
μ_{eff}	Effective viscosity (Pa s)
β	constant (=0.012)
R	Radius (m)

(*continued on next page*)

Peer review under responsibility of The Society of Naval Architects of Korea.
* Corresponding author.
** Corresponding author.
E-mail addresses: pouyan.talebizadehsardari2@nottingham.ac.uk (P. Talebizadehsardari), A.Keshmiri@manchester.ac.uk (A. Keshmiri).

https://doi.org/10.1016/j.ijnaoe.2024.100606
Received 17 February 2024; Received in revised form 27 June 2024; Accepted 29 June 2024
Available online 3 July 2024

(*continued*)

R_b	Bubble radius (m)
F	Empirical parameter
r_g	Volume fraction
$Rnuc$	The volume fraction of the nucleation sites
P_1	Inlet pressure
P_v	Vapour pressure
σ	Cavitation number
ϕ_d	Design flow coefficient
$\phi\psi_t$	Non-dimensional hydraulic power
γ	Inlet tip blade angle (deg)

1. Introduction

Cavitation is commonly an undesirable phenomenon in turbomachinery. Cavitation occurs when there is a rapid change in the flow pressure, which causes the liquid pressure to become lower than the vapour pressure, resulting in bubbly flows. This phenomenon is accompanied by detrimental consequences such as erosion and vibration in mechanical components and a significant decline in performance and efficiency. Various endeavors have been undertaken to enhance the impeller designs of centrifugal pumps in order to get superior efficiency and less vibration via the use of computational techniques and experimental verification (Wang et al., 2020).

Inducers are an effective method of preventing cavitation in pumps. A catalyser is a component placed upstream of the significant impeller inlet on a centrifugal pump; thus, raising the pump's interior pressure improves cavitation efficiency. The main differences between an inducer and a pump impeller are the smaller inlet angle, lower flow coefficient, fewer blades, sharper leading edges, and greater blade solidity. Aside from rocket pump feed systems, water jet propulsion, high-speed ships, and auxiliary power units for aircraft, inducers have also been applied for other applications.

One of the most common ways of suppressing cavitation is inducer. An inducer is a device used to improve a centrifugal pump's stability and durability. The inducer has thus been extensively studied to reduce pressure drop and increase centrifugal pump efficiency. Consequently, computational fluid dynamics (CFD) has also proven to be important for anticipating pump cavitation. Under different operating conditions, Jakobsen and Keller (1971) studied the optimal design of inducers to obtain high evacuation efficiency and maintain structural integrity. Guo et al. (2016) studied the catalyzer fin number's effects on a radial pump's anti-cavitation characteristics. The inducers with two, three, and four blades were studied, and it was revealed that a pump with a 3-fins catalyser has less vapour volume fraction and consequently an improved exterior and anti-cavitation efficiency.

Furthermore, Fu et al. (2017) reported that a higher pressure at the outlet of an inducer is related to tip clearance. They evaluated two different blade tip clearances experimentally. They revealed that a minor tip approval leads to a higher-pressure increase, improving hydraulic performance and increasing the head coefficient of the inducers. Excess tip vortex cavitation appears from the pressure part to the fin's evacuation section, as Okita et al. (2009) demonstrated. In consequence, the adjacent blade's leading edge experiences cavitation. As a result, the casing is blocked more frequently. D′ Agostino et al. (2008) conducted a condensed-order style for pre-design and efficiency analysis of turbopump inducers. An analysis of turbopump catalyzers' earliest design and functioning was performed by utilizing a reduced-order model. Their study was a proof of concept of the proposed model as a robust engineering solution (Bramanti, Cervone, & d'Agostino, 2007). Suppressing cavitation effects through novel designs, two studies have been performed to explore cavitation effects on the inducer's performance (Brennen, 2011, 2014). Brennen critically reviewed the phenomenon of cavitation and its effects on the pump performance and the role of the inducer as an anti-cavitation solution. More specifically, the behaviour of flow and cavitation in a helical inducer pump are investigated by Lakshminarayana (1982) and Stripling and Acosta (1962). In another effort by Okita et al. (2003), the impacts of cavitation behaviour in a cascade and an axial pump were examined numerically. Three-dimensional results showed that the pressure drop generated at the cavity closing redirects the surface flow near the sheet cavitation toward the casing. The industrial inducer consisting of three blades was simulated using computational fluid dynamics (CFD) by Flores et al. (2008), considering hydrodynamic head drop, and the results emphasised a dramatic influence of cavitation on the backflow structure. To explore the influence of the dynamic behaviour of a four-bladed inducer, a study was carried out numerically and experimentally by Lettieri et al. (2016). The study exhibited the formation and distribution of the vapour structure across the inducer. Furthermore, the paper also suggests that the relations between the leading edge and the tip vortex cavity can lead to the collapse of the sheet cavity. Also, Hydrofoils with different leading edges have been modelled by Coutier-Delgosha et al. (2002) and experimental results have been compared. In another study, Coutier-Delgosha et al. (2004) performed experimental and numerical investigations of a test pump in cavitating and non-cavitating situations. A work available by Xu et al. (2017) the transient characteristics of cavitation phenomena in a mixed-flow pump utilizing a renormalization group (RNG) turbulence technique and a Zwart-Gerber-Belamri cavitation technique. They reported that increasing the blade tip clearance from 0 to 1 mm decreases the head by 1.88 m, and the efficiency drops by 3.75%. Also, the critical net positive suction head (NPSHC) raised by 0.65 m, which was 4.8% of the NPSHC under no-tip clearance conditions. In addition to explained works, other researchers have studied rotating cavitation (Hadavandi, Pace, Valentini, Pasini, & d'Agostino, 2019; X. Li et al., 2013; Pace et al., 2017; Rakibuzzaman et al., 2018; Wang and Chang, 2010), flow structure (Fu et al., 2018; Mousmoulis et al., 2019; Choi et al., 2022), and turbulence in pumps with an inducer (Guo et al., 2015; Guo et al., 2015; Guo et al., 2015; Mejri et al., 2006).

Despite the number of works that have been accomplished to investigate the axial inducer performance numerically and experimentally, the role of geometrical and operational parameters of the axial inducers has not been scrutinized. Therefore, this work evaluated the mass transfer and cavitation actions of the inducer of motor pumps in various circumstances and customized a numerical simulation to achieve the ideal grouping of inducer tip clearance to mean blade height ratio, inlet tip blade angle, and surface roughness. It was anticipated that this research would contribute to the conceptual optimization study of inducer centrifugal pumps with high cavitation resistance. Considering the literature review, few studies have been achieved on the effects of these parameters on inducer non-cavitation and cavitation performances. For that purpose, a numerical framework is set by considering the governing equations for the mass and momentum and the additional transport formula for the turbulence model. Furthermore, the reliability of the framework is examined through a critical comparison against experimental data. As a result of the many contributing elements and causes of cavitation, our study aimed to optimize the cavitation efficiency and physical functioning of inducers.

2. Mathematical model

2.1. The physical model

The inducer includes a three-fined, tapered-hub, adjustable-pitch catalyser with model speed and flow coefficient of 2500 revelations/min and 0.059, respectively. The dimensions and operating factors of the model and the 3D inducer model are used in the simulations given in Table 1 and Fig. (1) (Pace et al., 2015).

2.2. Governing equations

Solving the conversation formulas for mass and momentum is required to resolve the stream inside the inducer. A turbulence model is also employed to account for the flow turbulent effect. Previous studies

Table 1
Structural and functioning features of the catalyser.

Model stream coefficient	0.06
Fins (blade) Num.	3
Tip diameter	16.2 cm
Interior tip fin angle	83.1°
Interior hub diameter (fully developed fin)	8.9 cm
Outlet hub diameter	11.7 cm
Axial length (fully developed blade)	6.35 cm
Mean fin elevation	2.95 cm
Rotational speed	2500 rev/min
Inlet hub diameter	7 cm
Axial dimension	9 cm
Diffusion element	0.39
The ratio between the rate and fin angles	0.3
Tip solidity	2.03
Hub solidity	2.07
Tip angle at the structure	2.07°
Exterior tip fin angle	74.58°

Fig. 1. A 3D view of the present inducer.

have shown the importance of the choice of the turbulence models on the accuracy of the results in Reynolds-Averaged Navier-Stokes (RANS) simulations (Keshmiri et al., 2012, 2016; Lopez-Santana et al., 2022). A steady incompressible turbulent flow can be modelled using the following equations:

$$\frac{\partial}{\partial x_j}\left(\rho U_j\right)=0 \tag{1}$$

$$\frac{\partial}{\partial x_j}\left(\rho U_i U_j\right)+\frac{\partial}{\partial x_j}\left(\rho\overline{u_i' u_j'}\right)=-\frac{\partial P}{\partial x_i}+\frac{\partial}{\partial x_j}\left(\mu\frac{\partial U_i}{\partial x_j}\right)+\rho f_i \tag{2}$$

where ρ is density, U denotes velocity vector, and μ is the fluid viscosity. The stress tensor ($-\rho\overline{u_i' u_j'}$) is modelled using the Boussinesq (1877) idea, which links the Reynolds stresses to the average velocities variations with the vortex viscosity (μ_t) as a ratio component.

$$-\rho\overline{u_i' u_j'}=\left[\mu_t\left(\frac{\partial U_i}{\partial x_j}+\frac{\partial U_j}{\partial x_i}\right)\right]-\frac{2}{3}\rho k\delta_{ij} \tag{3}$$

in which k is the turbulence dynamic energy. Finally, given the flow complexity and suggested model in the literature (Jafarzadeh et al., 2011; Li and Wang, 2007; Zhao et al., 2017), k-ε scheme was chosen as the best approach for the present study. Furthermore, it is important to emphasize that our prior research (Shojaeefard et al., 2019) extensively deliberated on the significance of selecting appropriate turbulence models. The dynamic energy of turbulence (k) and its dissipation rate (ε) are attained through the next conservation formulas:

$$\frac{\partial}{\partial x_j}\left(\rho U_j k\right)=\frac{\partial}{\partial x_j}\left(\frac{\mu_{eff}}{\sigma_k}\frac{\partial k}{\partial x_i}\right)+G_k-\rho\varepsilon \tag{4}$$

$$\frac{\partial}{\partial x_j}\left(\rho U_j \varepsilon\right)=\frac{\partial}{\partial x_i}\left(\frac{\mu_{eff}}{\sigma_k}\frac{\partial \varepsilon}{\partial x_i}\right)+C_{\varepsilon 1}G_k\frac{\varepsilon}{k}-\rho C_{\varepsilon 3}\frac{\varepsilon^2}{k} \tag{5}$$

where $\mu_{eff}=\mu_t+\mu$ is the efficient viscosity and $\mu_t\left(=\rho C_\mu\frac{k^2}{\varepsilon}\right)$ is the turbulent viscosity. The proportion consideration for the turbulent viscosity is C_μ, which is 0.085. $G_k\left(=-\rho\overline{u_i' u_j'}\frac{\partial U_j}{\partial x_i}\right)$ is the generation of turbulent kinetic energy due to the mean velocity gradients, and σ_k and σ_ε are the adequate Prandtl numbers for the turbulence kinetic energy and dissipation rate, respectively. Moreover, $C_{\varepsilon 3}$ is a grouping of $C_{\varepsilon 2}$ and R, which is defined as follows:

$$C_{\varepsilon 3}=C_{\varepsilon 2}+\underbrace{\frac{C_\mu\eta^3(1-\eta/\eta_0)}{1+\beta\eta^3}}_{R} \tag{6}$$

The typical generation part factor, $C_{\varepsilon 1}$(=1.4), and the dissipation part factor, $C_{\varepsilon 2}$(=1.7), are calculated theoretically using the RNG concept. The proportion of the turbulent period (k/ε) to the average strain rate (S) is known as $\eta(Sk/\varepsilon)$.

S is the measure of the deformation tensor given by $S=(2w_{ij}\,w_{ij})^{1/2}$, where $w_{ij}=\frac{1}{2}\left(\frac{\partial U_j}{\partial x_i}-\frac{\partial U_i}{\partial x_j}\right)$. The constant η_0(=4.38) is the constant part for the identical shear stream of the RNG k-ε technique formulas exclusive of R (attained in the limit of small w_{ij}). B which is equal to 0.012 is a fixed, which is calculated built on a connection with the von Karman constant (Hosseini et al., 2024; Zare et al., 2024). The scalable wall functions (Grotjans, Menter, & European Community on Computational Methods in Applied, 1998) are utilized to connect the solution factors at the near-wall cells and the subsequent numbers on the wall.

It is necessary to apply a cavitation model to calculate the rate of vapour production. A model based on the Rayleigh-Plesset (Plesset, 2021; Rayleigh, 1917) equation is applied in the present study. The Rayleigh-Plesset formula describes the increase of a gas bubble in a liquid, and is specified by:

$$R_b\frac{d^2R_b}{dt^2}+\frac{3}{2}\left(\frac{dR_b}{dt}\right)^2+\frac{2\sigma_t}{\rho R_b}=\frac{P_v-P}{\rho_f} \tag{7}$$

where R_b is the bubble radius, and σ_t is the surface tension constant between the liquid and vapour. p_v is the pressure in the bubble (the vapour pressure at the liquid temperature), p is the pressure in the liquid surrounding the bubble, and ρ_f is the liquid density. Neglecting the surface tension, this equation reduces to:

$$R_b\ddot{R}_b+\frac{3}{2}\dot{R}_b^{\,2}=\frac{P_v-P}{\rho_f} \tag{8}$$

The above nonlinear ordinary differential formula is difficult to implement within an Eulerian-Eulerian context for multi-phase flows, so the first-order calculation of the equation is applied where:

$$\dot{R}=\sqrt{\frac{3}{2}\frac{P_v-P}{\rho_f}} \tag{9}$$

The rate of changes in the bubble volume and the bubble mass are defined as follows:

$$\frac{dV_b}{dt}=\frac{d}{dt}\left(\frac{4}{3}\pi R_b^3\right)=4\pi R_b^2\sqrt{\frac{2}{3}\frac{P_v-P}{\rho_f}} \tag{10}$$

$$\frac{dm_b}{dt} = \rho_g \frac{dV_b}{dt} = 4\pi\rho_g R_b^2 \sqrt{\frac{2}{3}\frac{P_v - P}{\rho_f}} \tag{11}$$

If there are *Nb* bubbles per unit volume, the volume fraction, *rg*, can be expressed by $r_g = V_b N_b = \frac{4}{3}\pi R_b^3 N_b$. When the vapour volume fraction grows, the nucleation site density must reduce because there is a reduction of liquid. Consequently, the whole interphase mass transfer rate per volume is (Plesset, 2021; Rayleigh, 1917):

$$\dot{m}_{fg} = F\frac{3r_{nuc}(1 - r_g)\rho_g}{R_{nuc}}\sqrt{\frac{2}{3}\frac{|P_v - P|}{\rho_f}}sgn(P_v - P) \tag{12}$$

where *Rb* is replaced by *Rnuc* (=1 μm), *F* is an empirical parameter, which is assumed to be 50 for vaporisation, and r_{nuc} is the volume fraction of the nucleation places, which is considered 5×10^{-4}.

2.3. Boundary conditions

Appropriate boundary conditions are chosen for the computational domain such that at the entrance of the duct, an overall pressure is prescribed, as a velocity is imposed at the exit section. Furthermore, the counter-rotating wall state is directed to the casing. The considered field of the examined inducer is represented in Fig. 2. The employed boundary conditions for the numerical simulation are stated in the figure for various areas. It is shown that the assumed entire pressure is applied as the boundary condition at the inner section of the channel and a specified mass flow rate is employed at the outer section.

2.4. Mesh sensitivity analysis

The computational domain was meshed using unstructured tetrahedral elements. The mesh was generated by ANSYS ICEM (Version 16.1). The grid network is shown in Fig. 3(a) and (b). Applicable inner and outer lengths are accounted for to ensure a stable solution. The grid network at regions near the blades was refined to capture the complex flow with high-velocity gradients fully.

Six different grid densities were generated to test flow parameters and obtain a grid-independent result. Then, the head coefficients at the design point ($\phi = 0.059$) are explored for different mesh densities as compared in Table 2. Based on the results, the head coefficient increases for the higher mesh densities up to 612,530 computational cells, while beyond that number, slender changes are observed, which witnesses a grid-independent computational domain.

2.5. Solver settings

A numerical model is established using ANSYS-CFX (version 16.1). Finite volume methods are applied to the governing equations in CFX using an element-based approach. The velocity pressure was coupled using the SIMPLE scheme, and a high-determination second-order system was applied to compute the advection term. A turbulence intensity of 5% is considered appropriate for the flow at the duct inlet. To obtain a fully converged solution, a root mean square of 10-6 was used as the threshold for residuals.

3. Validation

An attempt is made to determine the validity of the numerical solution by comparing it to experimental data by Torre et al. (2009). Comparative analysis is conducted for non-cavitation and cavitation performances of the inducer, which can be characterized by the stream coefficient (ϕ), the direct coefficient (ψ), and the cavitation number (σ) as follows:

$$\psi = \frac{\Delta P}{\rho\Omega^2 r_T^2}$$
$$\phi = \frac{Q}{\rho\Omega r_T^3} \tag{13}$$
$$\sigma = \frac{P_1 - P_v}{0.5\rho\Omega^2 r_T^2}$$

where ΔP is the pressure difference between the inner and outer, P_1 is the inlet pressure, P_v is the vapour pressure, ρ is the fluid density, Ω denotes the inducer rotational speed, and r_T defines the inducer tip radius. The following will show the comparison of the non-cavitation and cavitation performances.

The stream coefficient, direct coefficient, and cavitation number are calculated based on the pressure difference between the inducer's inlet and outlet computed from CFD. The results are specific to a particular flow rate, which means they are point-specific. Because the mass flow rate is considered as the outlet boundary condition, the pressure difference will change as the mass flow rate changes.

As shown in Table 2, stream, direct coefficient, and cavitation number highly rely on the solution domain, mesh density, turbulence model, and other numerical simulation parameters. Depending on the mesh density and the turbulence model selected, the stream coefficients are extremely sensitive (Keshmiri et al., 2016). The accuracy of the direct coefficient depends on the accuracy with which flow rates are

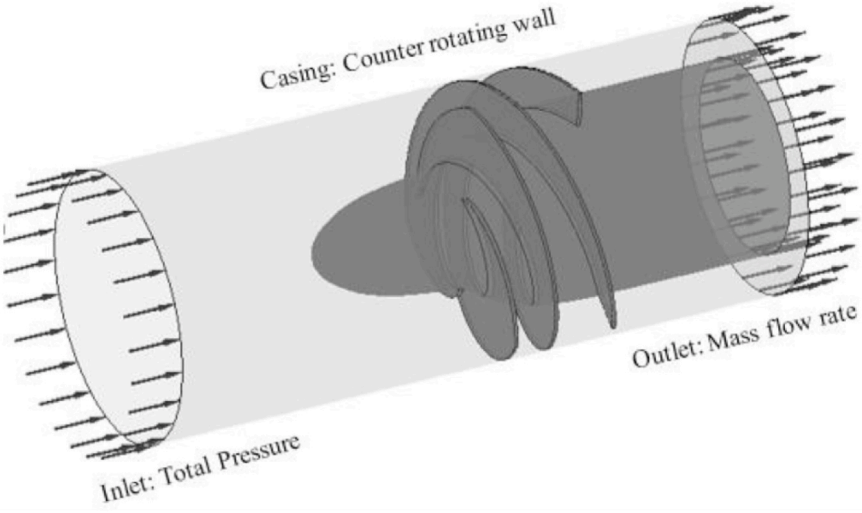

Fig. 2. Computational domain of the studied inducer.

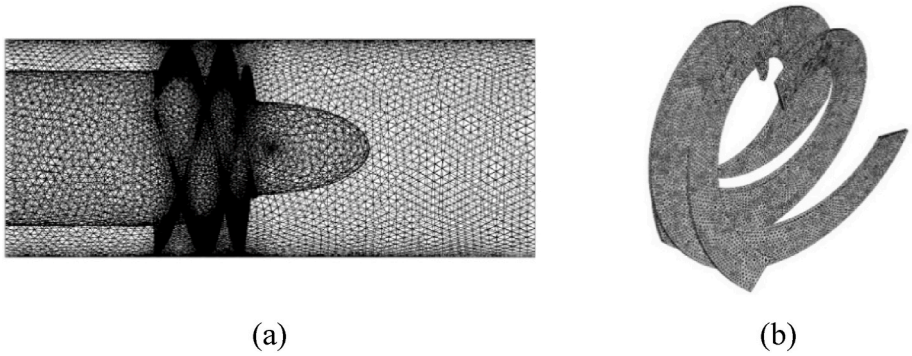

Fig. 3. The free grid of the entire computational field, including (a) the blade and (b) the inducer.

Table 2
Grid independency study.

No. of cells	186235	194260	259456	612530	787880	1354230
Head Coefficient	0.16893	0.19478	0.20006	0.20273	0.20271	0.20274
Number of Prism layers	15	15	15	15	15	15
Maximum Y^+	81	73	65	41	40	38
CPU time (s)	538	636	691	737	734	1133

calculated. In contrast, the cavitation number is strongly influenced by the region in which cavitation occurs. These factors ensure that the numerical calculations and the obtained coefficients are accurate and reliable. This improves the interpretability of inducer performance optimization results.

Fig. 4 illustrates the trend of the head and flow coefficients in non-cavitation conditions. It is worth mentioning that the results are achieved when the inlet pressure is constant and the velocity is variable. Two values for the tip clearance to mean blade height ratio, c% = 2.7 and 6.8, are considered for an inducer revolving velocity of 2500 rev/min and the water temperature of 19.2 °C. As a result of comparisons with experimental data, the maximum and average relative errors are 13.45% and 1.95% for c% = 2.7, and 10.73% and 3.19% for c% = 6.8, respectively. Hence, the numerical simulation can appropriately expect the flow conditions.

The computational and experimental outcomes show a slight difference in the head coefficient at high flow coefficients, approximately 0.044, whereas the disparity becomes greater at lower flow coefficients, where the numerical method slightly underestimates the head coefficient. The numerical solution is unstable in this region, making it

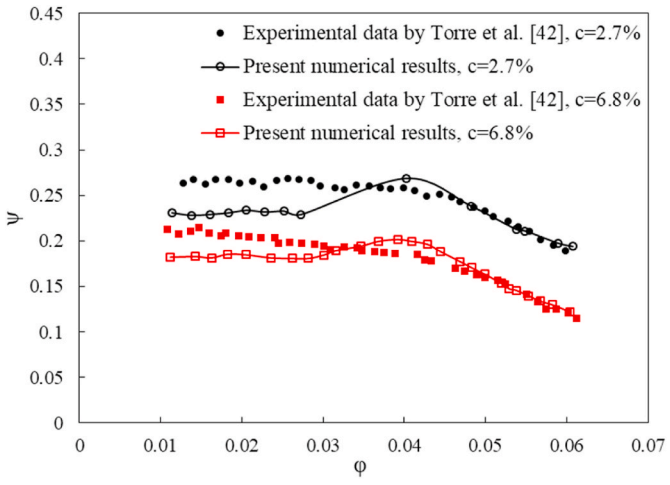

Fig. 4. Evaluation of the numerical results with the empirical data by Torre et al. (2009) for non-cavitation presentation.

unpredictable (Bakir et al., 2004; Li and Wang, 2007). Additionally, the head coefficient locally increases between ϕ = 0.035 and 0.045, which can be linked to the RANS limitation, which cannot capture the backflow region (Coutier-Delgosha et al., 2005; Keshmiri et al., 2008, 2016, 2015). Upon reaching half of the nominal amount, the head coefficient drop is around 2%, while it is less than 8% in the remaining portion of the curve.

Furthermore, the numerical head coefficient at some points is higher than that of the experimental one due to the omission of the impacts of gap flow over the channel side and some losses during the experimental assessment.

The numerical method's instability at lower flow coefficients presents obstacles to accurately estimating crucial performance metrics, such as the head coefficient. CFD simulations reveal this instability through oscillations or variations in the numerical solution, particularly in areas where the flow becomes highly unstable or exhibits complex behavior. The instability has a direct impact on the precision of forecasting the head coefficient since it introduces uncertainty and differences between computational forecasts and experimental data. More precisely, the numerical solution exhibits oscillatory behavior, causing variations from the expected patterns in the head coefficient. This effect is particularly noticeable at lower flow coefficients, where the flow conditions are more prone to instability. The consequences of this instability for engineering design and optimization are substantial. Erroneous forecasts of the head coefficient can lead to suboptimal designs, inefficient operational circumstances, and potentially expensive design errors. Engineers depend on computational models to direct the design and optimization processes. However, the existence of numerical instability weakens the dependability of these models, resulting in possible hazards and inefficiencies in real-world applications.

In general, at lower flow rates, the numerical model slightly overestimates the head coefficient. Numerical instability and the accuracy of the turbulence model account for the discrepancy at lower flow rates. The numerical results in other regions are highly accurate. As a result, the model performed particularly well at mid-range flow rates, where the numerical results matched the experimental data closely. Despite some deviations, the numerical model provides a reasonable approximation of pump performance under non-cavitation conditions.

Quantifying the deviations between numerical simulations and experimental data can be used to assess the accuracy of the model. However, the maximum relative errors indicate specific conditions

where the model's predictions deviate more significantly, even though the average relative errors are within an acceptable range, indicating overall reliability. Due to the complexity of flow dynamics at different tip clearances, it is difficult to capture these errors with accuracy. The reduction in tip clearance to mean blade height ratio will increase the backflow between the blade tip and the casing, resulting in a blockage that will likely negatively affect the solution's stability. However, these discrepancies do not undermine the overall confidence in our simulations, as most of the results are consistent with experimental data, particularly under critical operating conditions.

Moreover, based on different values of the tip clearance to mean blade height ratio, a similar trend is observed, and both the numerical and experimental results predict an increase in the inducer performance for higher ratios. Therefore, the inducer performance strongly depends on the tip permission to average fin height ratio as defined in Eq. (14), and the value should remain lower than 2% (Brennen, 2011).

$$\phi_l = \phi_h \sqrt{\frac{\psi_l}{\psi_h}} \tag{14}$$

where the subscripts l and h refer to lower and higher values of clearances, respectively.

Occasionally and given the inducer performance, cavitation may

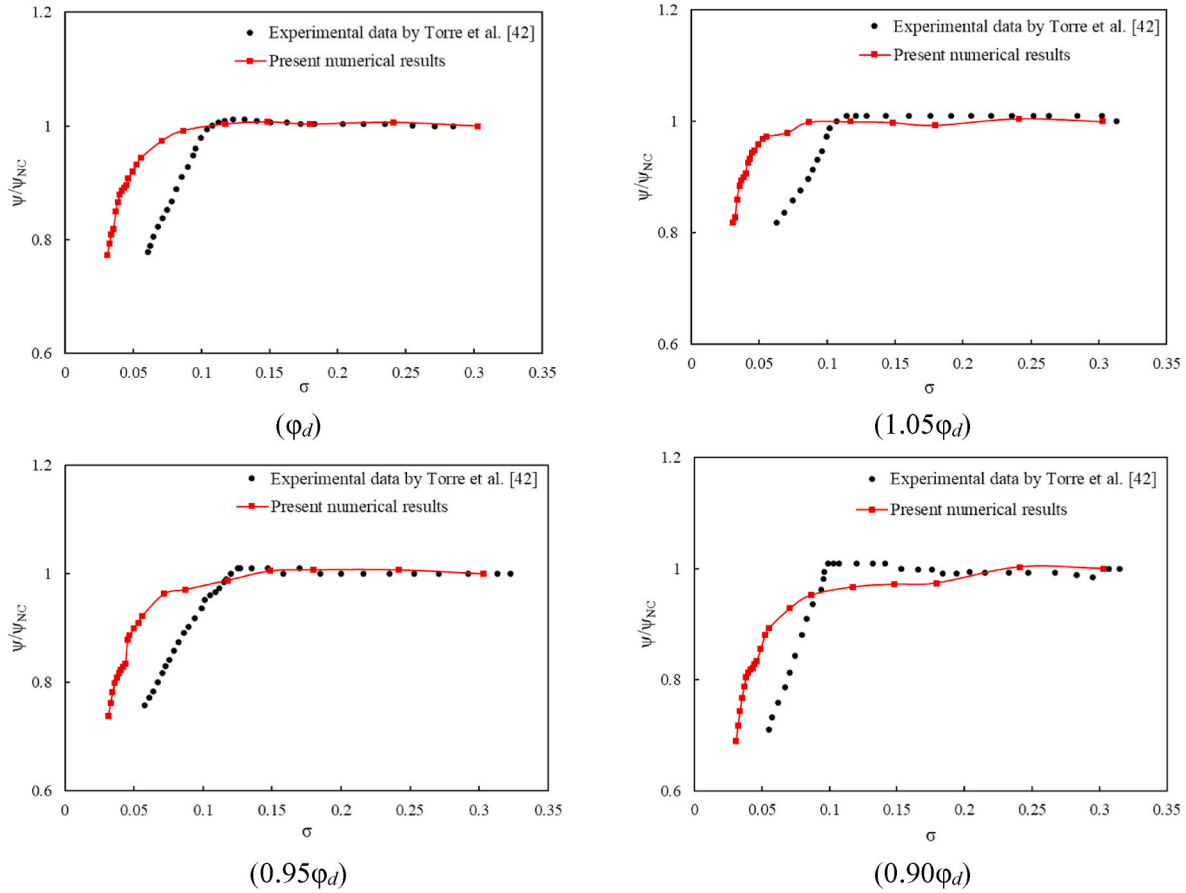

Fig. 5. (a) Comparison of the numerical results against the experimental data by Torre et al. (2009) for cavitation performance at different flow coefficients and (b) vapour distribution on the inducer blades.

occur. Therefore, the numerical model should be able to capture the phenomenon. For the cavitation performance case, the variations of the head coefficient against the cavitation number for the design condition ($\phi_d = 0.059$) and three off-design conditions ($0.9\phi_d$, $0.95\phi_d$ and $1.05\phi_d$) are shown in Fig. 5(a). The recreations are achieved for the inducer rotational speed of 3000 rev/min and the tip permission to average fin height ratio of 2.7%. Finally, the results are plotted for different flow coefficients within the range of atmospheric inlet pressure to the minimum reachable pressure.

For the simulated cases, the average relative errors concerning the experimental data are 5.68%, 7.35%, 4.07%, and 10.13% for ϕ_d, $1.05\phi_d$, $0.95\phi_d$ and $0.90\phi_d$, respectively. The numerical results demonstrate a similar trend to the experimental data; nevertheless, they predict lower suction performance within low mass flow rates.

Moreover, each graph in Fig. 5(a) demonstrates a critical cavitation number, below which the head coefficient drops rapidly by a slight decrease in cavitation number. A nearly straight line is obtained for the values above the critical cavitation number. The former underscores the emergence of cavitation inside the inducer, while the latter shows non-cavitation conditions. In terms of predicting the critical cavitation point at a design flow rate, the experimental and computational outcomes indicate an acceptable consistency. However, the numerical simulations predict higher critical cavitation values for lower flow rates and lower values for higher flow rates. Thus, it can be said that the computational model accurately estimates the point of critical cavitation near the nominal flow rate.

The main cause of these variations can be attributed to the constraints of the cavitation model employed in the computational simulations, specifically its failure to account for specific bubbles within the designated range of flow rates and its underestimation of mechanical losses. The Rayleigh-Plesset cavitation model, although commonly employed and acknowledged, may not sufficiently depict the behavior of all cavitation bubbles, particularly in situations characterized by lower flow rates as suggested by Wang et al. (2023). Moreover, the computer model's formulation may not adequately consider mechanical losses, which might have a substantial impact on the projected critical cavitation levels. Given these factors, it is suggested that enhancing and adjusting the cavitation model itself would be the most effective way to address the identified differences. By improving the model's representation of cavitation processes and adding ways to take into account bubbles and mechanical losses that were not taken into account before, it is possible to make the computer predictions more accurate without having to do more expensive research.

Although adjusting the mesh size in critical areas could improve the computational model's accuracy, it is important to acknowledge that this method may result in substantial costs in terms of computational resources and time. Furthermore, it might not effectively tackle the fundamental constraints of the cavitation model and could be considered unfeasible or redundant. Hence, the primary goal will be to refine the cavitation model in order to accurately correspond with empirical data, thereby improving our computer model's forecasting accuracy.

The vapour creation on the inducer blades for the flow factor of $\phi = 0.059$ is compared qualitatively between the numerical results and experimental data (Cervone et al., 2007). Based on the results, it is clear that cavitation (red zone) initially appears at the leading edge on the suction side of each blade. The further reduction of the cavitation number will result in an extension of the cavitation zone, which will seriously impair the performance of the inducer.

4. Results and discussions

Here are the parts; the effects of four parameters, i.e., tip clearance to mean blade height ratio, inlet tip blade angle, temperature, and surface roughness, are investigated in two different working conditions, i.e., cavitation and non-cavitation performances.

4.1. Effect of tip clearance to average fin height ratio

Non-cavitation performance: A comparison of the non-cavitation performance of the inducer with a tip clearance to an average fin height ratio is shown in Fig. 6. Fig. 6(a) and (b) display fluid velocity vectors for two different values of tip permission to an average fin height ratio ($c = 2.7\%$ and 6.8%) at two different flow coefficients.

At a relatively high value of c, 6.8%, the backflow region near the tip blades is more extended compared with $c = 2.7\%$. By increasing c, the maximum velocity increases; however, more flows will be separated at the tip blades. This phenomenon occurs due to the leakage between the tip blades and the shroud chamber. A backflow rotates rapidly around the inducer, and its development in the passages is explained by the differential pressure between the evacuation and pressure applied and the formation of vortices (Han et al., 2020).

At a nominal flow rate, the backflow forms slightly. When the flow rate is less than its optimum value, and the cavitation number is low, low-pressure zones and significant separations have been observed in the vicinity of the suction surfaces of the fin (Cheng et al., 2021). Furthermore, in reduced flow conditions, the tip flow goes upwards, creating a large backflow area (G. Li et al., 2022).

A static pressure distribution of the blades can be seen in Fig. 6(c) and (d). The leading edge of the blades (evacuation side) and the trailing edge (pressure section) have low and high-pressure regions. The results confirm a significant static pressure reduction caused by a rise in flow coefficient and the tip clearance to an average fin height ratio. Additionally, static pressure increases as the blades progress from their inlet to their outlet.

Fig. 6(a–d) provide valuable insights for designing the most effective inducer to enhance non-cavitation performance. Through the examination of pressure distribution and backflow across the figures, we can determine the arrangement that exhibits the least amount of backflow and the most efficient pressure recovery. This is presumably associated with a particular blade shape or flow coefficient. These findings can be used to prioritize design characteristics that promote an optimal pressure distribution in future inducers. Once the trends have been found, they may be used to direct specific design optimization efforts through simulations or experiments. This will lead to a further reduction of backflow and an improvement in pump efficiency. Ultimately, incorporating the enhanced design into a fresh prototype and verifying its performance enables gradual enhancement, drawing from the observations made in Fig. 6(a–d).

c has a significant impact on the inducer's non-cavitation performance because it influences flow patterns and velocity distribution. An increased clearance (greater c) leads to a higher leakage flow, resulting in a decrease in pressure rise and efficiency. Additionally, it stimulates secondary currents that disturb the primary current and result in energy dissipation. Moreover, a greater clearance can result in an uneven distribution of velocity around the blades, which may lead to separation and an additional decrease in efficiency. Thus, a reduced clearance (decreased c) is typically favored. Nevertheless, the production and upkeep of extremely narrow gaps pose difficulties due to the risk of friction and erosion. The ideal value of c entails achieving a harmonious equilibrium between efficient hydraulic performance and feasible production constraints.

Variations of the hydraulic efficiency for different values of flow coefficient are plotted in Fig. 7(a), using Eq. (15).

$$\eta = \frac{Q\Delta P_t}{\tau\Omega} \tag{15}$$

As clearly shown, for both values of c, an increase in the flow coefficient will increase the hydraulic efficiency. Based on the results, it appears that by raising the flow factor, the increasing volumetric flow rate compensates for the reduced pressure difference to inducer torque ratio due to the increased flow factor. Furthermore, for higher values of c, the hydraulic efficiency slightly reduces.

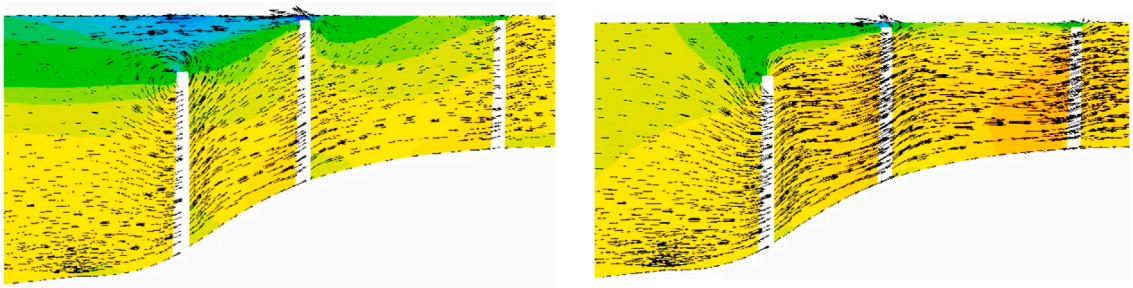

φ=0.027, *c*=2.7% φ=0.059, *c*=2.7%

(a)

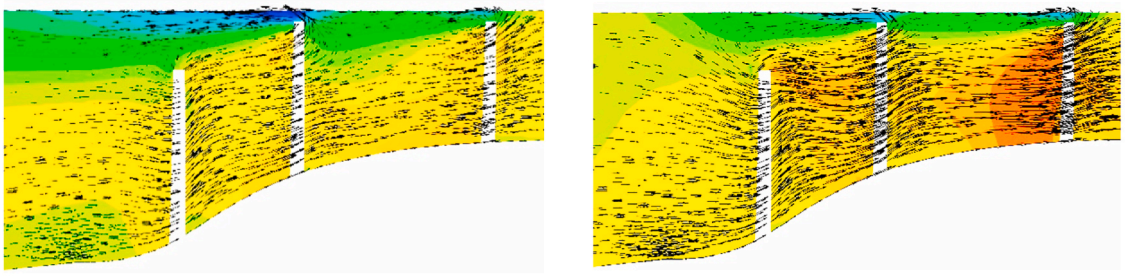

(c) φ=0.027, *c*=6.8% (d) φ=0.059, *c*=6.8%

(b)

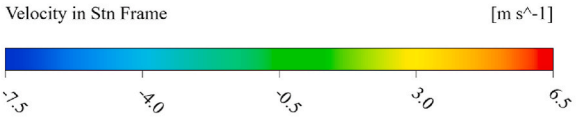

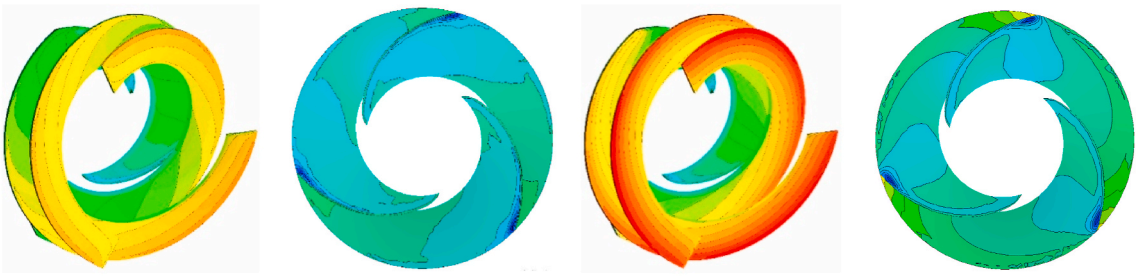

φ=0.027, *c*=2.7% φ=0.059, *c*=2.7%

(c)

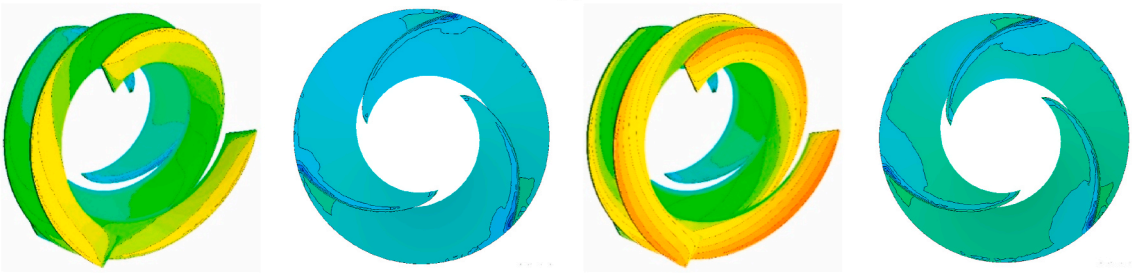

φ=0.027, *c*=6.8% φ=0.059, *c*=6.8%

(d)

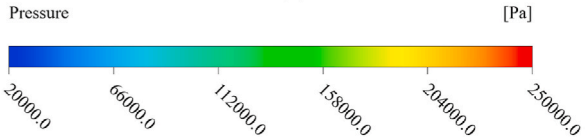

Fig. 6. (a) The distributions of the liquid water velocity for $c = 2.7\%$ and (b) 6.8%, and (c) comparison of the static pressure distributions of blades for $c = 2.7\%$ and (d) 6.8% at $\phi = 0.027$ an $\phi = 0.059$ for 2500 rec/min.

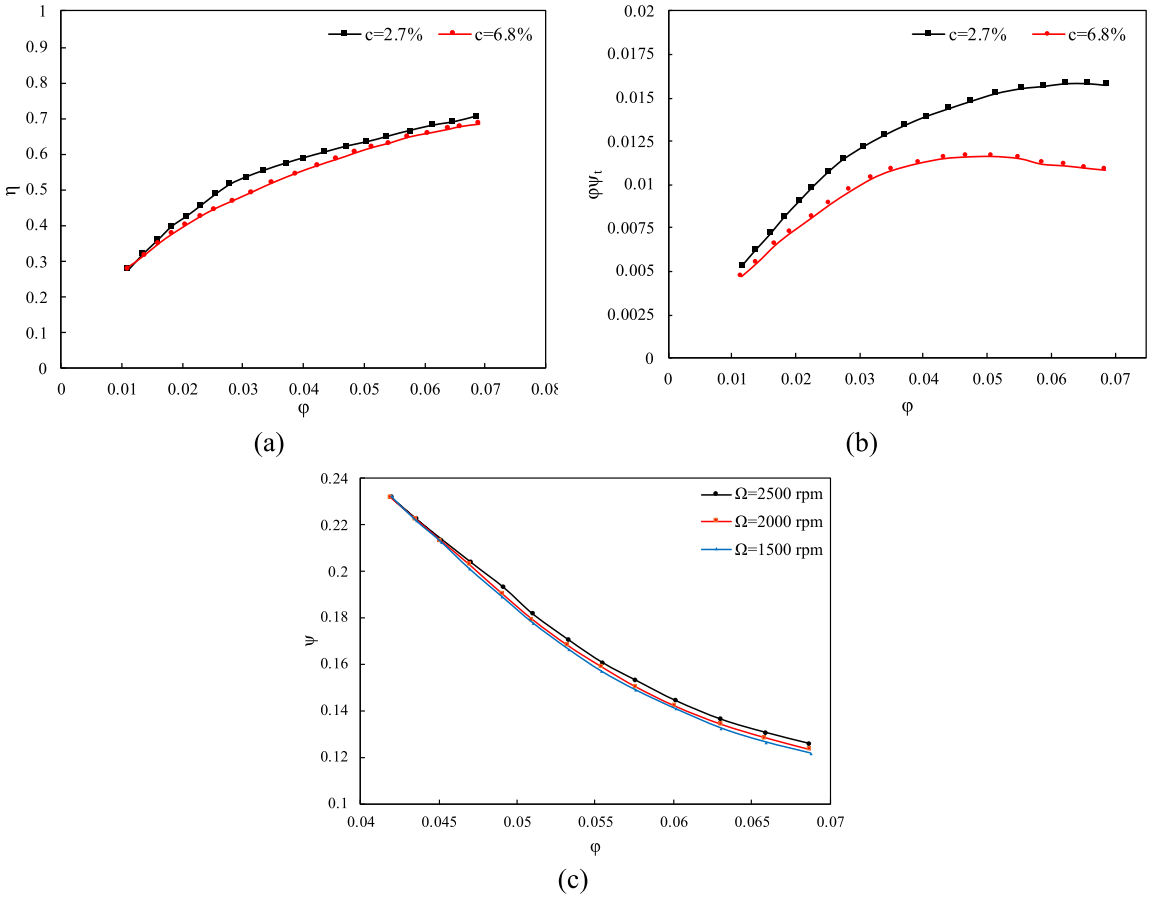

Fig. 7. Effects of tip clearance to mean blade height ratio on inducer (a) hydraulic efficiency and (b) hydraulic power at the rotational velocity of 2500 rev/min, and (c) effect of rotational speed on the non-cavitation efficiency of inducer.

Fig. 7(b) demonstrates the non-dimensional hydraulic power of the inducer as defined by Eq. (16).

$$\phi\psi_t = \phi\frac{\Delta P_t}{\rho\Omega^2 r_T^2} \tag{16}$$

For both c values and within the studied range, the hydraulic power initially increases and reaches a plateau. Additionally, higher c value results in a declined hydraulic power. The maximum hydraulic power for $c = 2.7\%$ occurs at $\phi = 0.068$, while for $c = 6.8\%$, it occurs earlier, at $\phi = 0.05$. The cause of the increase in hydraulic power is the increase in total pressure difference. This is low when partial flow coefficients are low and increases as flow coefficients increase.

Fig. 7(c) shows the inducer performance under three rotational speeds. The results are obtained at three rotational speeds of 1500, 2000, and 2500 rev/min for the water temperature of 19.2 °C and tip permission to an average fin height ratio of 6.8%. Based on the results, there is almost no difference between the characteristic curves, and the rotational velocity slightly influences the inducer efficiency. Because of the fully turbulent nature of the flow, the performance is independent of the Reynolds number ($Re = 2\Omega {r_T}^2/\nu$). Moreover, the inducer head reduces by increasing the flow coefficient, as depicted in Fig. 3.

Cavitation performance: It is examined how tip clearance and mean blade height ratio affect cavitation performance under four different conditions (Fig. 8). The simulations are run at design conditions and for a rotational velocity of 3000 revelations/min and water temperature of 17.3 °C. The outcomes suggest that the head coefficient behaviour is independent of the tip clearance to an average fin height ratio at the cavitation region. The cavitation number, however, rapidly decreases after reaching the critical cavitation number. Additionally, the head coefficient reduces at the non-cavitation region by increasing the tip clearance to the mean blade height ratio.

As a result of an increase in c at the cavitation field, the critical cavitation number decreases, and the head performance drop is delayed. However, there is a trade-off between the c value, cavitation occurrence, and head coefficient. The results of the near-curved knee demonstrate that the optimal amount of tip clearance is 1% of the chord, which generally corresponds with the cavitation radius influence of the tip blade.

Although a bigger tip clearance (higher c) may appear to exacerbate cavitation, it can actually prolong its initiation by decreasing the overall pressure drop in the inducer. Nevertheless, there is a price to pay for this. A greater clearance results in the formation of a larger low-pressure area around the tip, increasing its vulnerability to cavitation once it initiates. Determining the ideal clearance includes a delicate equilibrium: prolonging the initiation of cavitation for effective functioning necessitates a higher clearance, but this can exacerbate the subsequent effects of cavitation. Conversely, a lower clearance decreases the vulnerable tip area but may result in quicker cavitation initiation. In addition, narrower clearances provide greater challenges in terms of manufacturing and maintenance. The ultimate goal is to develop a clearance that effectively balances these considerations while also preserving optimal head performance. This may entail employing computer modeling or conducting tests to evaluate the effects of various clearances on cavitation behavior, head performance, and overall pump efficiency.

The present numerical findings are evaluated against the experimental outcomes of Cervone et al. (2009) for the cavitation occurrence across the inducer at the nominal flow coefficient, water temperature of 19.2 °C, and rotational velocity of 3000 rev/min. Accordingly, Fig. 8

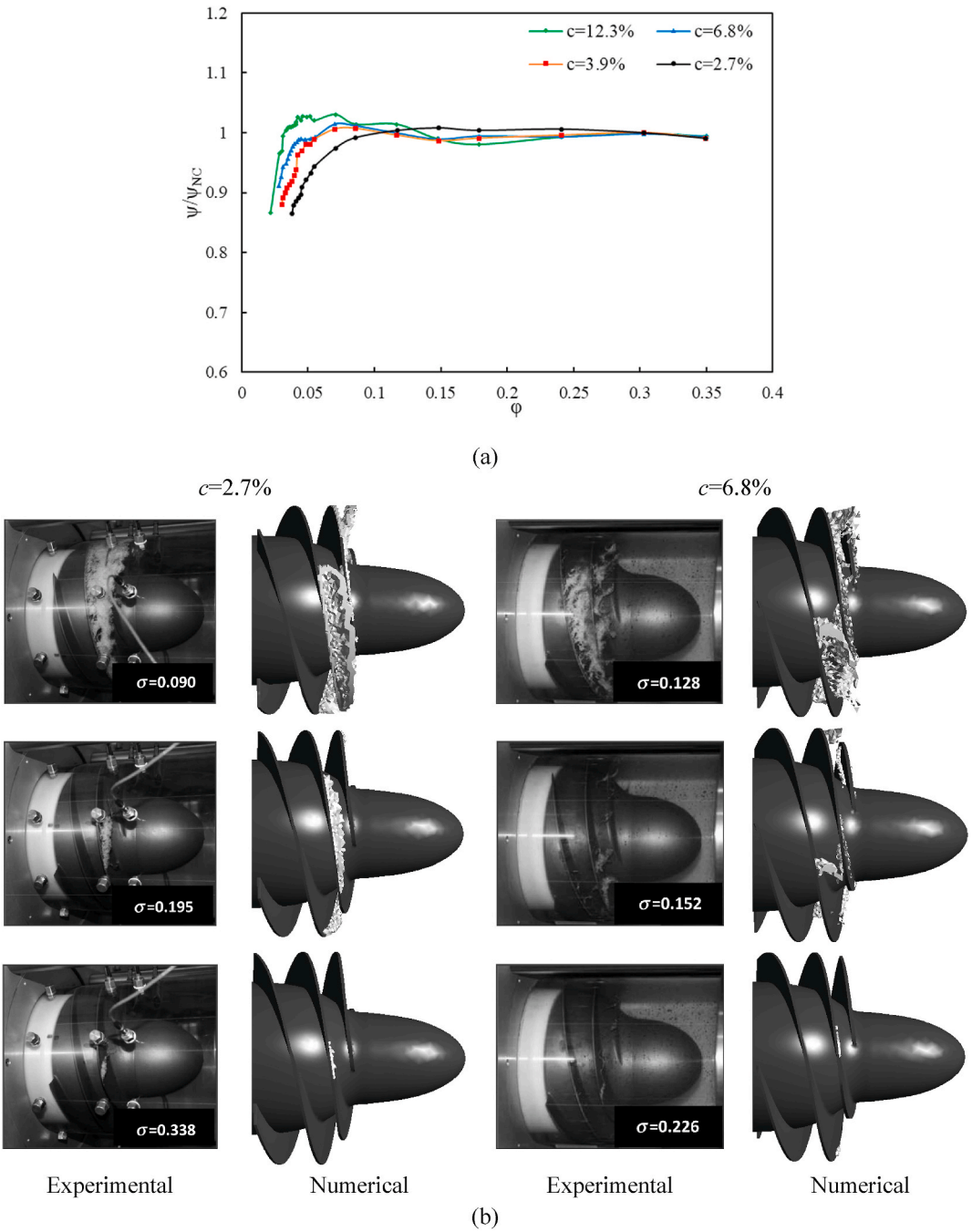

Fig. 8. (a) effect of tip clearance to mean blade height ratio on inducer cavitation performance and (b) comparison of the experimental results by Cervone et al. (Cervone et al., 2009) and numerical results of the appearance of the cavitation on the inducer under design condition, rotational velocity of 3000 rev/min and water temperature of 17.3 °C.

illustrates three cavitation numbers for two different values of c. The numerical and experimental data are aligned reasonably in the comparison, mainly when cavitation numbers are high. The comparison shows that by decreasing the cavitation number, cavitation sheets form at each blade's leading edge ($\sigma = 0.338$, $c = 2.7\%$ and $\sigma = 0.226$, $c = 6.8\%$). Additionally, there is a further reduction in cavitation number in the cavitation zones, which appear on both the blades and the hub. Notably, the cavitation regions at the higher value of c are more chaotic, and it tends to dissipate flow upstream due to the higher backflow intensity. Exploring further the results for $\sigma = 0.09$ and 0.128 reveals that the vapour zones become larger and occupy the space between the blades and the tip clearance. The highest drops, which occur at low values of the cavitation number, significantly influence the head coefficient of the inducer. This behaviour can be linked to gradually generating blockage at the flow upwind (Zhang et al., 2022).

The occurrence of blockage at low cavitation number values, which leads to notable decreases in the head coefficient, can be attributed to many underlying mechanisms that are closely connected to the creation and extension of vapour zones between the blades and tip clearance. When the cavitation numbers are low, the pressure inside the inducer falls, causing the cavitation to begin. When the pressure in a specific area drops below the fluid's vapour pressure, vapour bubbles form. The coalescence of these vapour bubbles can lead to the formation of vapour zones, which can disturb the flow patterns and result in blocking consequences. As the vapour zones expand, they cause blockages in the flow path, increasing obstruction and consequently decreasing the head

coefficient. Furthermore, the existence of vapour zones causes changes in the pressure distribution around the blades, leading to flow separation and subsequent losses. These phenomena together degrade the performance and efficiency of the inducer when subjected to cavitation conditions. The presence of vapour zones creates extra resistance and modifies the flow characteristics, diminishing the inducer's efficiency in producing pressure and transporting fluid within the system. In addition, the existence of vapour bubbles can cause instabilities in the flow, which worsen the decline in performance and efficiency. This has been further confirmed by He et al. (2023), who specifically investigated the prediction of cavitation dynamics in a twisted hydrofoil. To come up with effective ways to lessen the negative effects of cavitation on performance and improve the design of inducers for better performance in cavitation environments, it is important to fully understand these mechanisms.

4.2. Effect of inlet tip fin angle

This part examines the fin angle's impact at a catalyzer's inlet tip on cavitation and non-cavitation condition. Eight different blade angles are investigated, while other geometrical specifications are kept constant, as presented in Table 1.

Non-cavitation performance: Variations of the head performance against the stream coefficient for different inlet tip blade angles are presented in Fig. 9(a). The inducer rotational speed and water temperature are 2500 rev/min and 19.2 °C, respectively. Following the experimental findings, the head coefficient decreases with increasing flow coefficient (Torre et al., 2009).

Results of the study indicate a similar trend for various blade angles. However, high-angle inlet tip blade inducers experience a higher head coefficient value of around 85°. An optimal angle can be achieved by increasing the inlet tip blade angle (Shojaeefard et al., 2019); while other inducer design parameters are kept constant, the performance will be improved noticeably. Fig. 9(b) presents the hydraulic efficiency versus flow coefficient for different inlet tip blade angles. Findings suggest that the hydraulic efficiency reduces for higher values of inlet tip blade angle. The hydraulic performance is directly related to the total pressure variations to torque ratio, so the ratio increases at a lower inlet tip blade angle, resulting in improved hydraulic efficiency. Whereas, since the head coefficient is just correlated to the total pressure difference, it increases due to the higher angle of the inlet tip blade.

According to Fig. 9(b), the analysis of hydraulic efficiency versus flow coefficient for different inlet tip blade angles indicates that variations in blade angles significantly impact fluid dynamics and pump performance. It is believed that lower inlet tip blade angles result in smoother flow patterns and reduced hydraulic losses, which enhance efficiency. As a result of higher blade angles, turbulence, and backflows are increased, which reduces efficiency even when initial pressure rise and cavitation resistance are improved.

By reducing the incidence losses at the blade's entrance and the blockage effects at the blade's exit, the incidence losses at the entrance of the blades are reduced. Due to the increased pressure difference between the suction and pressure surfaces, more backflows occur at the tip blades, but these losses are relatively small, and the overall inducer performance improves as a result of the optimized head coefficient (Shojaeefard et al., 2019).

The profiles of the velocity streamlines at the nominal flow coefficient are depicted in Fig. 10(a) for three different inlet tip blade angles. A vital backflow region characterizes the first blade, whereas the pressure variation between the evacuation and pressure sides causes irregular backflow foci between the blades. Furthermore, backflow regions are more dominant when the inlet tip blade angle increases. Fig. 10, similar to the previous section, illustrates the static pressure distributions on the evacuation and pressure supply for different flow coefficients and blade angles at the inlet tip. As well understood, Low-pressure zones can be observed on the evacuation sides around the fins' leading edges, where cavitation is more likely to occur.

Moreover, various flow coefficient does not change the general pattern of different blade angles. There is a rise in static pressure as the blades move from the inlet to the outlet, and a decrease in the inlet tip blade angle results in a dramatic reduction in static pressure. Furthermore, similar pressure distribution patterns can be observed across the blades, and the slight difference is owing to the non-uniform flow field created by the suction action.

Fig. 10 illustrates low-pressure zones around the fins' leading edges, which may result in surface erosion, increased vibration, and reduced hydraulic efficiency due to cavitation. A pressure drop occurs at the blade tips as a result of backflow and blockages. Cavitation occurs when this pressure falls below the fluid's vapour pressure, resulting in the formation of bubbles. It is possible to mitigate these effects by optimizing blade design, applying cavitation-resistant coatings, operating the pump under optimal conditions, using advanced materials that are resistant to erosion, and implementing flow control devices.

Cavitation functioning: As explained in Fig. 11, the inlet tip blade angle affects the cavitation functioning of the catalyzer. The results are reported for the design condition and at the spin velocity of 3000 rev/min, the water temperature of 17.3 °C, and the tip permission to average fin height ratio of 2.7%.

The head coefficient curves show the same trends for all inlet tip blade angles. From $\sigma = 0.1$ to 0.3, the head coefficient remains almost constant (non-cavitation zone), and a blade angle of 85° at the inlet tip of the inducer shows appropriate performance than the other inducers in

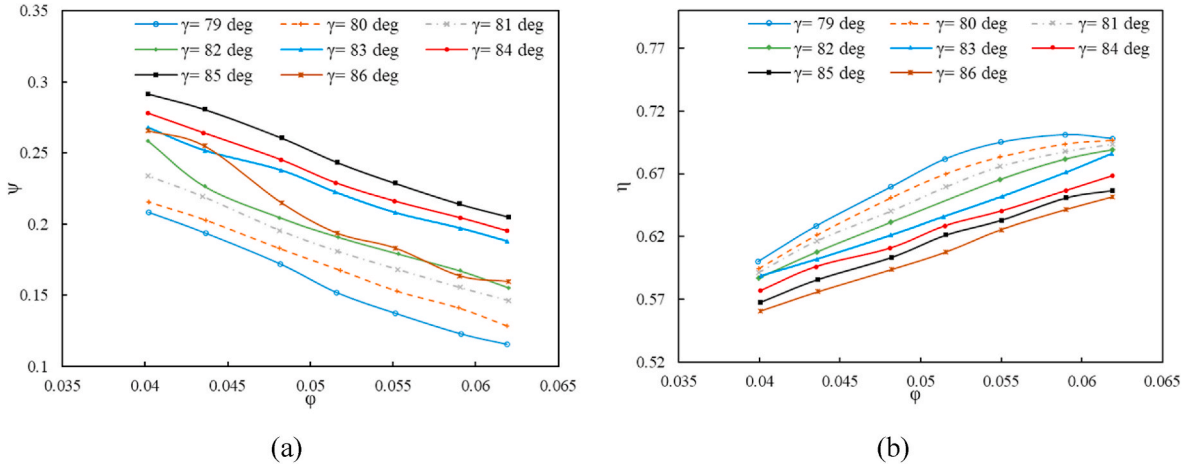

Fig. 9. Effect of inlet tip blade angle on (a) inducer non-cavitation performance and (b) inducer hydraulic efficiency.

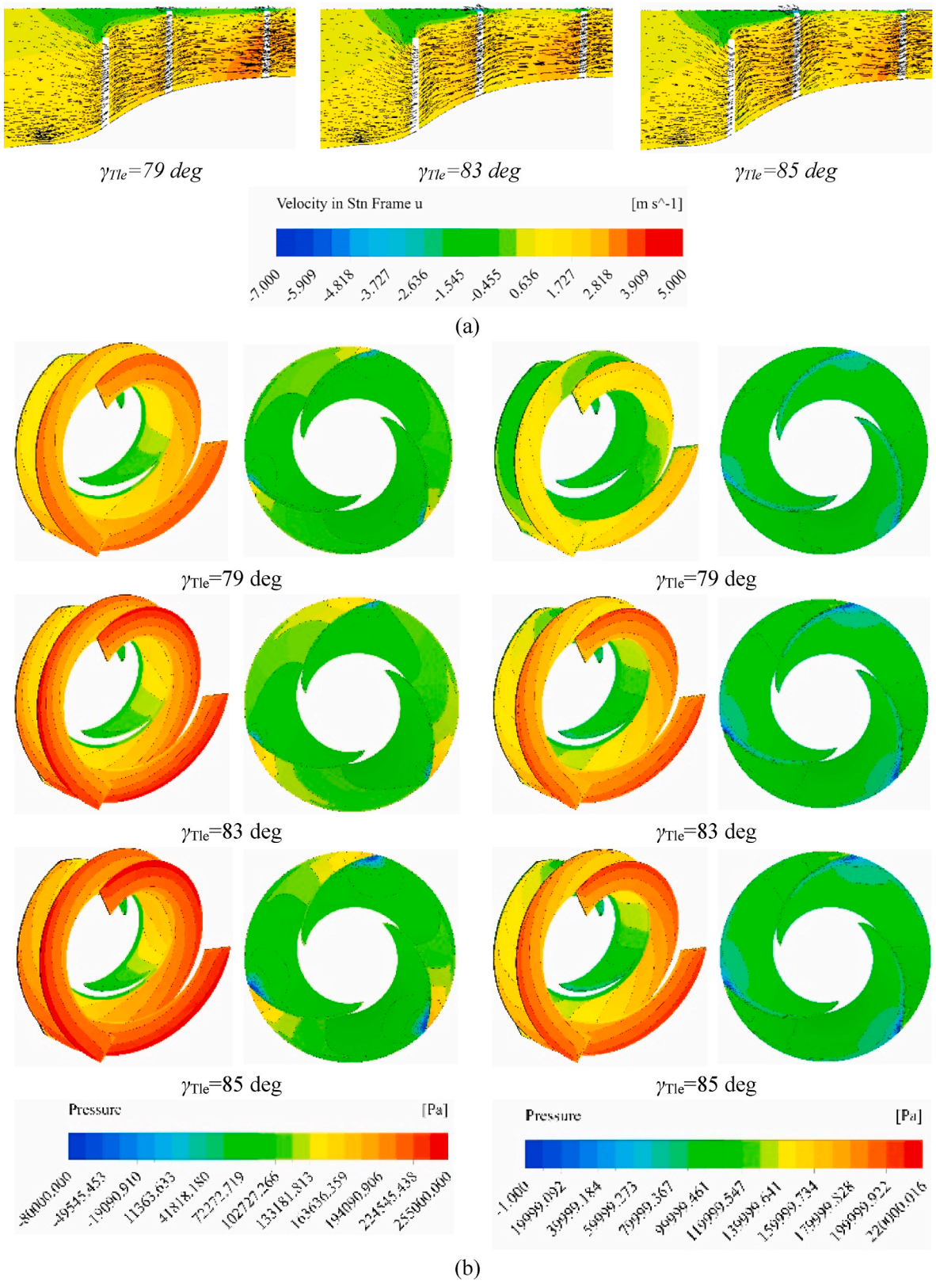

Fig. 10. (a) Comparison of (a) the distributions of liquid water velocity and (b) the static pressure distribution of blades at different inlet tip blade angles at the nominal flow coefficient.

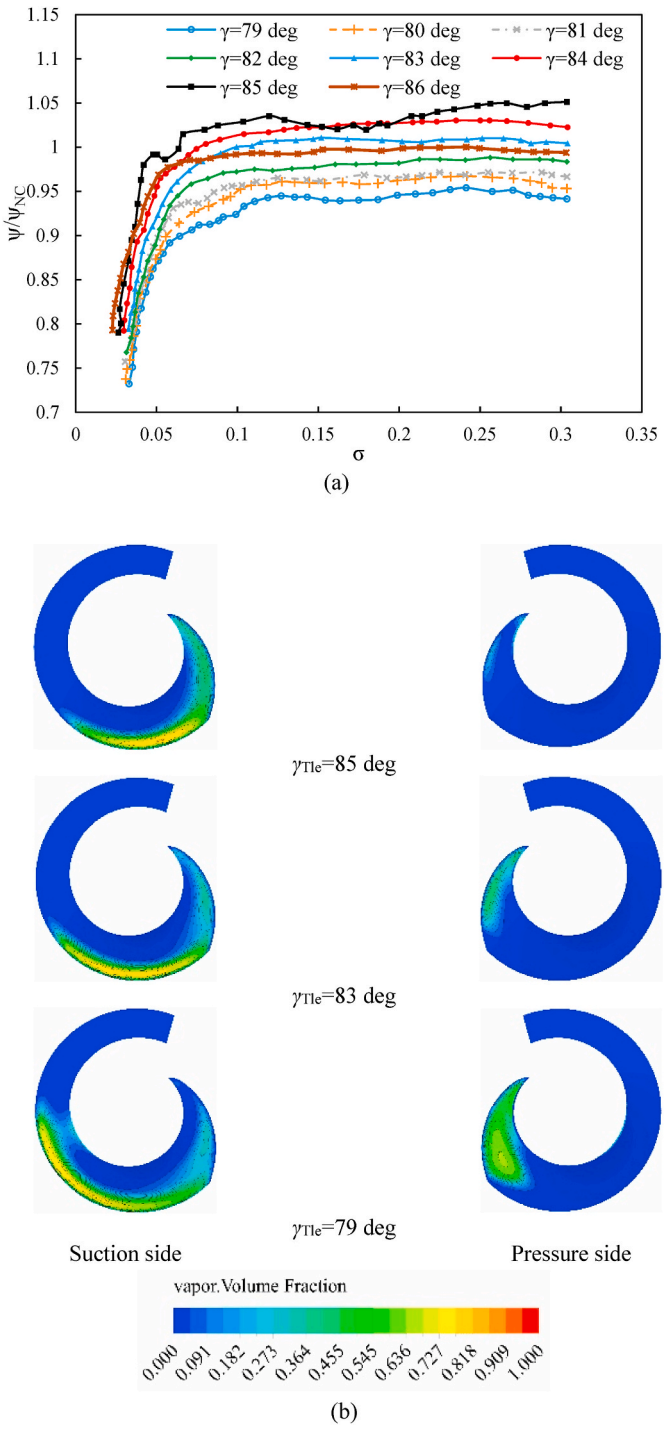

Fig. 11. (a) Effect of inlet tip blade angle on inducer cavitation performance, and (b) comparison of vapour volume fraction for different inlet tip blade angles at suction side and pressure side of inducer blades.

this region. After reaching the critical cavitation number, the inducer performance significantly reduces. At high inlet pressure (non-cavitation state), the head is not affected, whereas by decreasing the pressure, cavitation appears and is aggravated gradually in the inducer, leading to the head decrease. It needs to say that σ is the ratio of pressure head to vapour pressure, values ranging from 0.1 to 0.3 indicate an adequate amount of pressure to effectively avoid cavitation formation. Thus, rather than cavitation, the head coefficient remains consistent, determined by the shape of the inducer and the operating circumstances. Even if σ remains constant, there may be performance changes. Varying blade angles can have an impact on the flow characteristics inside the inducer. A certain angle could provide a more ideal trajectory, resulting in modest changes in efficiency relative to other angles. This may appear as slight variations in pressure distribution or energy dissipation. Examining pressure and velocity profiles at various blade angles may reveal potential efficiency differences.

Observation reveals that cavitation breakdown declines with rising inlet tip blade angle. Also, there is a sudden drop in the head performance curve at inlet tip blade angles of 81 and 85°, just before the breakdown, where the cavitation number drops even further. It can be explained that by increasing the inlet tip blade angle to a specific value, the pressure at this area elevates, and the flow coefficient is improved at the blade entrance, resulting in better cavitation performance. Beyond this angle, the blade entrance passageway is blocked with more increments of the inlet tip blade angle. Therefore, the flow coherence undermines, leading to a decline in cavitation performance. This behavior indicates an intricate interaction between the blade angle, cavitation formation, and fluid movement within the inducer. As the cavitation number drops, nearing the threshold of cavitation breakdown, the intensity of cavitation can intensify. This results in a greater amount of liquid undergoing vaporisation, which leads to a substantial decrease in the effective flow area via the inducer. This constricted pathway may significantly reduce the pressure increase (head coefficient) that the inducer achieves. In addition, when the blade angles are set at specified values, such as 81° and 85°, the interaction between the blade and the incoming flow can enhance the occurrence of secondary flows within the inducer. The presence of secondary flows may result in additional energy losses and disturbances to the primary flow, thereby exacerbating the decline in head performance. Under exceptional circumstances, the interaction of cavitation and secondary flows may result in flow separation near the blade tip. This division can cause a substantial section of the blade to lose its effectiveness, leading to a large decrease in the head coefficient. The abrupt decrease in head coefficient is anticipated to occur immediately prior to reaching the critical cavitation number for the specified blade angles. This shows a key point where the effects of cavitation expansion, secondary flows, and potential flow detachment become too strong for the inducer to keep working at its best.

Fig. 11 illustrates the water vapour volume fraction profiles at a sample blade's suction and pressure sides for $\sigma = 0.037$. Again, the formation of vapour zones at the leading edge can be observed at both sides, but the vapour zone is lower at the pressure side and extends towards a larger blade area by decreasing the inlet tip blade angle.

4.3. Effect of temperature

It is valuable to know that the temperature of the working fluid has a meaningful impact on the performance of inducers (Hosseini and Keshmiri, 2022). This section investigates the effect of temperature on the inducer's non-cavitation and cavitation performances for different temperatures of 10, 25, 40, and 60 °C.

Non-cavitation performance: changes in the fluid temperature that is pumped affect the fluid density, vapour pressure, and dynamic viscosity. By considering the representative curve of the inducer's performance and assuming a rotational speed of 2500 rev/min and tip permission to average fin height ratio of 2.7%, Fig. 12(a) illustrates the effect of the operating fluid temperature on its non-cavitation efficiency.

The results show that the temperature rise slightly improves the performance. Therefore, the available evidence suggests that fluid temperature has little impact on the performance of the inducer under non-cavitation conditions.

Fig. 12(a) demonstrates a notable pattern: the non-cavitation efficiency increases slightly as the temperature of the operating fluid rises. This indicates that the inducer exhibits somewhat superior performance at elevated temperatures, even in the absence of cavitation. Two fundamental aspects contribute to this enhancement. Firstly, as the

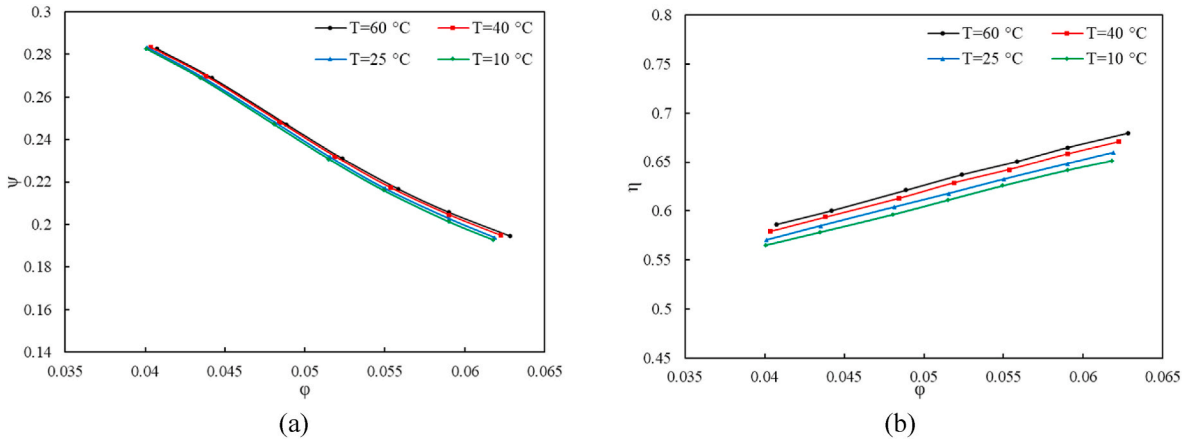

Fig. 12. Effect of water temperature on inducer (a) non-cavitation performance and (b) hydraulic efficiency for non-cavitation performance.

temperature rises, the viscosity of the fluid generally decreases. Reducing a fluid's viscosity results in a decrease in internal friction, which in turn leads to a minor reduction in energy losses within the inducer. This leads to a marginal increase in total efficiency. Furthermore, the choice of inducer material can result in thermal expansion, which in turn may cause a modest reduction in the gaps between the spinning and stationary parts. Decreasing the gaps between components can reduce the amount of fluid that escapes, which has the potential to enhance efficiency. Nevertheless, it is crucial to bear in mind that this impact is probably insignificant and must be assessed according to the precise characteristics of the material. In general, Fig. 12(a) indicates a direct relationship between non-cavitation efficiency and the temperature of the operating fluid within a specified range. The decrease in fluid thickness and the possibility of small alterations in the gaps between components can explain this. Nevertheless, the extent of this enhancement is expected to be minimal, and additional variables must be taken into account while establishing the ideal working temperature for the inducer.

In non-cavitation performance, empirical data indicates that the temperature of the fluid has a negligible effect on the inducer's performance. Understanding the fundamental components that influence non-cavitation performance is crucial to comprehending this. The inducer's configuration, including its blade design and flow routes, as well as operational parameters such as rotational speed and flow rate, determines how it interacts with the fluid. These immutable traits remain unchanged despite temperature fluctuations. In situations where cavitation is not present, the fluid's density and incompressibility, which determine how it interacts with the inducer, are not significantly affected by changes in temperature within the normal working range. Thus, temperature variations in non-cavitation zones substantially do not alter factors such as head coefficient, governed by geometry and operating circumstances, and primary flow patterns, determined by blade design. This investigation specifically examines conditions when cavitation does not occur. The influence of temperature on performance becomes more pronounced when cavitation occurs at elevated temperatures.

The hydraulic performance of the inducer is also illustrated in Fig. 12 (b). As displayed, by increasing the temperature, the hydraulic efficiency increases. This can be attributed to the slight change in the total pressure difference with temperature rise, while the inducer torque decreases due to the density reduction.

Fig. 12(b) illustrates a notable pattern: hydraulic efficiency improves a little as the fluid temperature increases, even in the presence of cavitation. The enhancement can be ascribed to a pivotal element: decreased fluid viscosity. As the temperature rises, the fluid's viscosity typically decreases, resulting in less internal friction within the inducer. The decrease in energy losses caused by friction leads to a small enhancement in overall hydraulic efficiency. Nevertheless, it is essential to take into account the consequences of decreasing viscosity in conjunction with the repercussions of cavitation. Elevated temperatures can occasionally exacerbate cavitation, potentially amplifying energy losses associated with bubble creation and burst. Furthermore, temperature variations may affect the cavitation position in the inducer, exacerbating energy losses. Although there are possible disadvantages, the decrease in viscosity may still be more important than the adverse effects of cavitation in certain situations, resulting in an overall enhancement in efficiency as temperature increases within a particular range. It is crucial to keep in mind that the degree of enhancement is expected to be minimal, and there is likely a specific temperature range that maximizes efficiency."

Cavitation performance: Using an inducer rotational speed of 3000 rev/min and tip permission to an average fin height ratio of 2.7%, we examined the impact of water temperature on inducer cavitation performance. The alteration in the water temperature affects the vapour pressure, thereby influencing the cavitation number. As illustrated in Fig. 13(a), the critical cavitation number decreases by increasing the temperature. In fact, for the same volume growth rate, the mass rate of evaporation increases due to an increase in vapour density. Subsequently, a thermal boundary layer is formed on the liquid side of the boundary, lowering the temperature inside the bubble well below the temperature of the bulk liquid. This means that the vapour pressure inside the bubble drops significantly, reducing the driving force behind bubble growth (Arndt, 1981; Chivers, 1969).

According to Fig. 13(a), the critical cavitation number decreases as water temperature increases, increasing the occurrence of cavitation. As a consequence, the trend is primarily the result of higher vapour pressures at high temperatures, which diminishes the pressure threshold triggering cavitation, and reduced viscosities, which increase turbulence intensity and local pressure differences. This phenomenon is also influenced by slight water density reductions. Inducer operation at higher temperatures requires careful monitoring and control to minimize the risk of cavitation. In addition to optimized blade angle and materials resistant to cavitation erosion, operational adjustments may involve reducing pump rotational speed or maintaining greater inlet pressures. To ensure reliability and avoid unexpected failures due to increased cavitation susceptibility, regular maintenance, and real-time monitoring are essential.

Fig. 13(b) also illustrates the distributions of the vapour volume fraction across the evacuation side (a) and pressure side (b) of the fin for different mentioned conditions. The results are obtained for the cavitation number of 0.037. Comparing different occurred scenarios, it can be shown that the minimum and the maximum vaporisation occur for water temperatures of 60 °C (suction side) and 40 °C (pressure side), respectively.

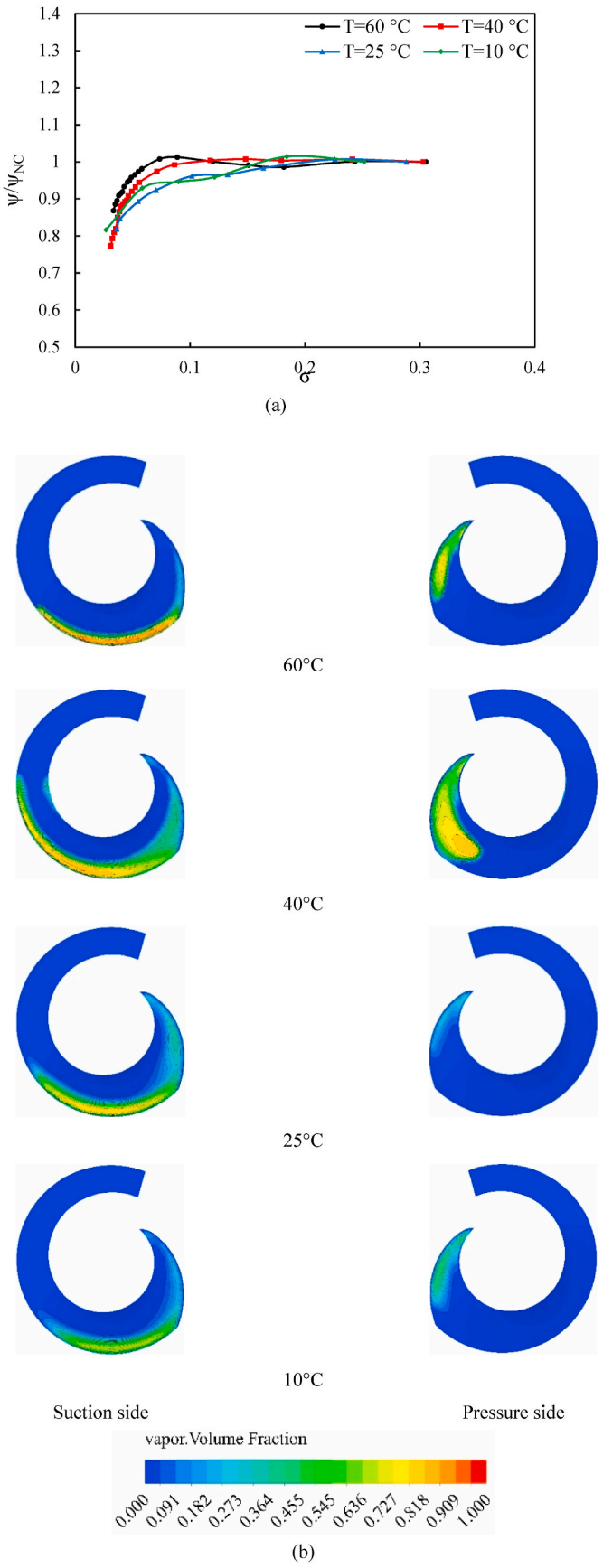

Fig. 13. (a) Effect of water temperature on inducer cavitation performance, and (b) comparison of vapour volume fraction for the variable liquid temperature at suction side and pressure side of inducer blades.

Based on the findings presented in this study, inducer design and operation will be significantly impacted. By understanding the impact of inlet tip blade angle, static pressure distribution, and temperature on cavitation, inducer performance can be optimized and cavitation effects effectively mitigated. Designers need to select blade angles that minimize turbulence and backflow, select materials that resist cavitation erosion, and apply surface treatments that reduce friction to minimize turbulence and backflow. It is imperative to manage thermal conditions effectively to maintain optimal fluid temperatures. To further stabilize flow patterns, flow control devices such as vortex breakers or inducer casings can be incorporated. Regular inspections and advanced monitoring technologies are required to maintain inducer performance and prevent extensive damage.

4.4. *Effect of the surface roughness*

Using sand grain roughness walls (k_s) as an example, we discuss how surface roughness affects inducer non-cavitation performance. According to Fig. 14(a), single-phase flow simulations result in a head coefficient versus a flow coefficient. The results are illustrated for the rotational velocity of 2500 rev/min and water temperature of 19.2 °C. To explore the roughness effects, slip surface conditions and five different surface roughness ($k_s = 0$, 25, 50, 100, 150 μm) are considered.

Based on the results, the head coefficient decreases as the flow coefficient increases. As a result of friction and volumetric losses, there is a similar trend in all cases. At partial loading conditions, volumetric losses dominate, whereas frictional losses dominate at high flow rates. According to the computational outcomes, the head coefficient decreases as the surface roughness increases. The latter implies that inducer surface roughness predominantly influences the head coefficient, which amplifies frictional losses.

Since the dependence of friction losses on the Re, the surface roughness effect can be observed explicitly in high flow coefficients (Limbach and Skoda, 2017). Therefore, it can be concluded that the greatest head coefficient is determined by the slip surface (Svennberg et al., 2020).

Changing the surface roughness of the inducer affects the vapour pressure; consequently, cavitation occurs. Hence, the impacts of surface roughness on the inducer cavitation efficiency are illustrated in Fig. 14 (b). It shows the cavitation performance of the inducer under nominal flow coefficient, spin velocity of 3000 rev/min, and water temperature of 17.3 °C. Accordingly, the head coefficient reduces by increasing k_s; however, the critical cavitation number does not change notably.

5. Conclusion

In this research, we analyzed the effect of various inducer structural characteristics on mass transfer and the development of cavitation under varying operating circumstances using the CFD numerical simulation approach. The accuracy of the simulations was demonstrated by the fact that the model predictions were in acceptable agreement with the experimental data. The current work numerically explored the effects of tip permission to average fin height ratio, inlet tip blade angle, surface roughness, and working fluid temperature on an axial inducer performance and the bubble spreading within the inducer stream duct and the streamline in the flow duct are attained.

The following main conclusions can be drawn from the study.

- Low pressure in the tip blades spreads into the flow channel, increasing the bubble dispersion, while minor vortices in the stream duct block the flow path.
- The static pressure and hydraulic efficiency decrease as the ratio of tip permission to average fin height increases in non-cavitating conditions. Also, extended backflow domains are seen around the tip blades, which revolve around the inducer with a positive proportion of the rotational speed velocity. Increasing the tip clearance

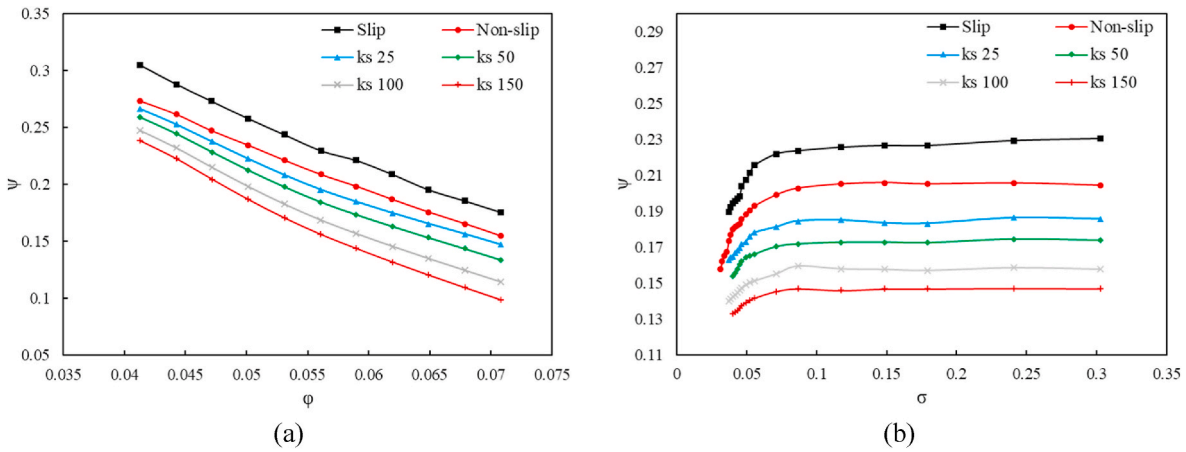

Fig. 14. Effect of surface roughness on inducer (a) non-cavitation performance for spin velocity of 2500 rev/min and water temperature of 19.2 °C and (b) cavitation performance at nominal flow coefficient, spin velocity of 3000 rev/min and water temperature of 17.3 °C.

ratio to mean blade height decreases the critical cavitation number in cavitation conditions, delaying the head coefficient decline.

- Because the curves are independent of the Reynolds number, the spin velocity only maximizes the catalysers' efficiency performance.
- In the absence of cavitation, the catalyzer with the greater inlet tip blade angle experiences a higher head factor until the inner tip fin angle reaches 85°, at which point the head factor decreases. Additionally, the hydraulic performance decreases, and the highest value of the hydraulic efficiency is associated with a lower inlet tip blade angle. The flow channel is smaller in blades with a higher inlet tip blade angle, and bubbles cannot spread smoothly throughout the stream duct, reducing cavitation resistance efficiency.
- As the working fluid temperature rises under non-cavitation and cavitation circumstances, the hydraulic efficiency increases while the cavitation breakdown reduces.
- Increasing surface roughness decreases the head coefficient under non-cavitation and cavitation circumstances; hence, a slip surface will produce the best results.
- While adding an inducer significantly impacts the pump's pressure difference and hydraulic efficiency, it can dramatically reduce the pump's cavitation, underlining the need for further inducer design optimization.

Declaration of competing interest

The authors declare that they have no known competing financial interests or personal relationships that could have appeared to influence the work reported in this paper.

Acknowledgment

The corresponding author, Dr. Amir Keshmiri would like to acknowledge the funding by the UK Engineering and Physical Sciences Research Council (EPSRC – Reference: EP/X525753/1) under the Impact Acceleration Account (IAA) provided to the University of Manchester, which has supported the underpinning research in this study.

References

Arndt, R.E.A., 1981. Cavitation in fluid machinery and hydraulic structures. Annu. Rev. Fluid Mech. 13 (1), 273–326. https://www.annualreviews.org/doi/abs/10.1146/annurev.fl.13.010181.001421, 10.1146/annurev.fl.13.010181.001421.

Bakir, F., Rey, R., Gerber, A.G., Belamri, T., Hutchinson, B., 2004. Numerical and experimental investigations of the cavitating behavior of an inducer. Int. J. Rotating Mach. 10, 690740 https://doi.org/10.1155/S1023621X04000028, 10.1155/S1023621X04000028.

Boussinesq, J., 1877. *Essai sur la théorie des eaux courantes*: Imprimerie Nationale.

Bramanti, C., Cervone, A., d'Agostino, L., 2007. A simplified analytical model for evaluating the noncavitating performance of axial inducers. Paper Presented at the 43rd AIAA/ASME/SAE/ASEE Joint Propulsion Conference & Exhibit.

Brennen, C.E., 2011. Hydrodynamics of Pumps. Cambridge University Press.

Brennen, C.E., 2014. Cavitation and Bubble Dynamics. Cambridge university press.

Cervone, A., Bramanti, C., Torre, L., Fotino, D., d'Agostino, L., 2007. Setup of a high-speed Optical system for the Characterization of flow instabilities generated by cavitation. J. Fluid Eng. 129 (7), 877–885. https://doi.org/10.1115/1.2742738, 10.1115/1.2742738.

Cervone, A., Torre, L., Pasini, A., dÀgostino, L., 2009. Cavitation and flow instabilities in a 4-bladed axial inducer designed by means of a reduced order analytical model. In: 47th AIAA/ASME/SAE/ASEE Joint Propulsion Conference & Exhibit.

Cheng, H.-y., Ji, B., Long, X.-p., Huai, W.-x., Farhat, M., 2021. A review of cavitation in tip-leakage flow and its control. J. Hydrodyn. 33 (2), 226–242. https://doi.org/10.1007/s42241-021-0022-z.

Chivers, T., 1969. The correlation of cavitating performance for a centrifugal pump handling various liquids. Archive: Proceedings of The Institution of Mechanical Engineers 1847-1982 (vols 1-196) 184, 48–68. https://doi.org/10.1243/PIME_PROC_1969_184_009_02.

Choi, J.K., Kim, H.T., Lee, C.S., Lee, S.J., 2022. A numerical investigation on head losses and flow qualities for a large cavitation tunnel without impeller. Int. J. Nav. Archit. Ocean Eng. 14, 100494 https://doi.org/10.1016/J.IJNAOE.2022.100494.

Coutier-Delgosha, O., Reboud, J.-L., Fortes-Patella, R., 2002. Numerical study of the effect of the leading edge shape on cavitation around inducer blade sections. JSME International Journal Series B Fluids and Thermal Engineering 45 (3), 678–685. https://doi.org/10.1299/jsmeb.45.678.

Coutier-Delgosha, O., Fortes-Patella, R., Reboud, J.L., Hofmann, M., Stoffel, B., 2004. Experimental and numerical studies in a centrifugal pump with two-dimensional curved blades in cavitating condition. J. Fluid Eng. 125 (6), 970–978. https://doi.org/10.1115/1.1596238, 10.1115/1.1596238.

Coutier-Delgosha, O., Morel, P., Fortes-Patella, R., Reboud, J.L., 2005. Numerical simulation of turbopump inducer cavitating behavior. Int. J. Rotating Mach. 2005, 752538 https://doi.org/10.1155/IJRM.2005.135, 10.1155/IJRM.2005.135.

d'Agostino, L., Torre, L., Pasini, A., Baccarella, D., Cervone, A., Milani, A., 2008. A reduced order model for preliminary design and performance prediction of tapered inducers: comparison with numerical simulations. In: Paper Presented at the 44th AIAA/ASME/SAE/ASEE Joint Propulsion Conference & Exhibit.

Flores, N.G., Goncalvès, E., Patella, R.F., Rolland, J., Rebattet, C., 2008. Head Drop of a Spatial Turbopump Inducer.

Fu, Y., Yuan, J., Yuan, S., Pace, G., d'Agostino, L., 2017. Effect of tip clearance on the internal flow and hydraulic performance of a three-bladed inducer. Int. J. Rotating Mach. 2017.

Fu, Y., Fan, M., Pace, G., Valentini, D., Pasini, A., d'Agostino, L., 2018. Experimental and numerical study on hydraulic performances of a turbopump with and without an inducer. Paper Presented at the ASME 2018 5th Joint US-European Fluids Engineering Division Summer Meeting.

Grotjans, H., Menter, F.R., 1998. European Community on computational methods in applied, S. In: Wall Functions for General Application CFD Codes. Paper Presented at the 4th, Vol 1 Pts 1-2; Proceedings of the Fourth European Computational Fluid Dynamics Conference. Chichester, Athens.

Guo, X., Zhu, L., Zhu, Z., Cui, B., Li, Y., 2015a. Numerical and experimental investigations on the cavitation characteristics of a high-speed centrifugal pump with a splitter-blade inducer. J. Mech. Sci. Technol. 29 (1), 259–267. http://inis.iaea.org/search/search.aspx?orig_q=RN:47111155.

Guo, X., Zhu, Z., Cui, B., Huang, Y., 2015b. Anti-cavitation performance of a splitter-bladed inducer under different flow rates and different inlet pressures. Sci. China Technol. Sci. 58 (12), 2131–2138. https://doi.org/10.1007/s11431-015-5928-7, 10.1007/s11431-015-5928-7.

Guo, X., Zhu, Z., Cui, B., Li, Y., 2015c. Effects of the short blade locations on the anti-cavitation performance of the splitter-bladed inducer and the pump. Chin. J. Chem.

Eng. 23 (7), 1095–1101. https://doi.org/10.1016/j.cjche.2015.03.002. https://www.sciencedirect.com/science/article/pii/S1004954115000920.
Guo, X., Zhu, Z., Cui, B., Shi, G., 2016. Effects of the number of inducer blades on the anti-cavitation characteristics and external performance of a centrifugal pump. J. Mech. Sci. Technol. 30, 3173–3181.
Hadavandi, R., Pace, G., Valentini, D., Pasini, A., d'Agostino, L., 2019. Identification of cavitation instabilities on a three-bladed inducer by means of strain Gages. J. Fluid Eng. 142 (2) https://doi.org/10.1115/1.4045186, 10.1115/1.4045186.
Han, C.-z., Xu, S., Cheng, H.-y., Ji, B., Zhang, Z.-y., 2020. LES method of the tip clearance vortex cavitation in a propelling pump with special emphasis on the cavitation-vortex interaction. J. Hydrodyn. 32 (6), 1212–1216. https://doi.org/10.1007/s42241-020-0070-9, 10.1007/s42241-020-0070-9.
He, P., Li, Z., Liu, Q., Zhang, X., He, W., 2023. Prediction of cavitation dynamics and cavitation erosion around a three-dimensional twisted hydrofoil with an LES method. Int. J. Nav. Archit. Ocean Eng. 15, 100536 https://doi.org/10.1016/J.IJNAOE.2023.100536.
Hosseini, S.E., Karimi, O., AsemanBakhsh, M.A., 2024. Experimental investigation and multi-objective optimization of savonius wind turbine based on modified non-dominated sorting genetic algorithm-II. Wind Eng. 48, 446–467. https://doi.org/10.1177/0309524X231217726.
Hosseini, S.E., Keshmiri, A., 2022. Experimental and numerical investigation of different geometrical parameters in a centrifugal blood pump. Research on Biomedical Engineering 38 (2), 423–437. https://doi.org/10.1007/s42600-021-00195-8, 10.1007/s42600-021-00195-8.
Jafarzadeh, B., Hajari, A., Alishahi, M.M., Akbari, M.H., 2011. The flow simulation of a low-specific-speed high-speed centrifugal pump. Appl. Math. Model. 35 (1), 242–249. https://doi.org/10.1016/j.apm.2010.05.021. https://www.sciencedirect.com/science/article/pii/S0307904X10002271.
Jakobsen, J.K., Keller, Jr R., 1971. Liquid Rocket Engine Turbopump Inducers. NASA SP-8052, 98 pages. Published by NASA, Washington, D.C.
Keshmiri, A., Addad, Y., Cotton, M.A., Laurence, D.R., Billar, F., 2008. Refined eddy viscosity schemes and large eddy simulations for ascending mixed convection flows. In: Proceedings of the Proc. 4th Int. Symp. On Advances in Computational Heat Transfer, "CHT08", Paper CHT-08-407; Marrakech, Morocco, vol. 44, pp. 1–22.
Keshmiri, A., Cotton, M.A., Addad, Y., Laurence, D., 2012. *Turbulence Models and large eddy simulations Applied to ascending mixed convection flows*. Flow. Turbul. Combust. 89, 407–434. https://doi.org/10.1007/s10494-012-9401-4.
Keshmiri, A., Revell, A., Darabkhani, H.G., 2016. Assessment of a common nonlinear eddy-viscosity turbulence model in capturing laminarization in mixed convection flows. Numer. Heat Transf. Part A Appl. 69 https://doi.org/10.1080/10407782.2015.1069672.
Keshmiri, A., Uribe, J., Shokri, N., 2015. Benchmarking of Three Different CFD Codes in Simulating Natural , Forced and Mixed Convection Flows. Numer. Heat Transf. Part A Appl. 2015, 67. https://doi.org/10.1080/10407782.2014.965115.
Keshmiri, A., Osman, K., Benhamadouche, S., Shokri, N., 2016. Assessment of advanced RANS models against large eddy simulation and experimental data in the investigation of ribbed passages with passive heat transfer. Numer. Heat Tran. Part B Fundam 69. https://doi.org/10.1080/10407790.2015.1096641.
Lakshminarayana, B., 1982. Fluid Dynamics of Inducers—A Review.
Lettieri, C., Spakovszky, Z., Jackson, D., Wang, V., 2016. Characterization of rotating cavitation in a four bladed inducer. Paper Presented at the 52nd AIAA/SAE/ASEE Joint Propulsion Conference.
Li, Y.-j., Wang, F.-j., 2007. Numerical investigation of performance of an axial-flow pump with inducer* *Project supported by the National nature Science Foundation of China (grant No. 90510007). Journal of Hydrodynamics, Ser. B 19 (6), 705–711. Beijing Nature Science Foundation of China (Grant No. 3071002) and the National Key Technology R and D Program (Grant No. 2006BAD11B07). https://www.sciencedirect.com/science/article/pii/S1001605808600074, 10.1016/S1001-6058(08)60007-4.
Li, X., Yuan, S., Pan, Z., Yuan, J., Fu, Y., 2013. Numerical simulation of leading edge cavitation within the whole flow passage of a centrifugal pump. Sci. China Technol. Sci. 56 (9), 2156–2162. https://doi.org/10.1007/s11431-013-5311-5, 10.1007/s11431-013-5311-5.
Li, G., Ding, X., Wu, Y., Wang, S., Li, D., Yu, W., Guo, Y., 2022. Liquid-vapor two-phase flow in centrifugal pump: cavitation, mass transfer, and impeller structure optimization. Vacuum 201, 111102. https://doi.org/10.1016/j.vacuum.2022.111102. https://www.sciencedirect.com/science/article/pii/S0042207X22002317.
Limbach, P., Skoda, R., 2017. Numerical and experimental analysis of cavitating flow in a low specific speed centrifugal pump with different surface roughness. J. Fluid Eng. 139 (10) https://doi.org/10.1115/1.4036673, 10.1115/1.4036673.
Lopez-Santana, G.B., Kennaugh, A., Keshmiri, A., 2022. Experimental techniques against RANS method in a fully developed turbulent pipe flow: Evolution of experimental and computational methods for the study of turbulence. Fluids 7 (2).
Mejri, I., Bakir, F., Rey, R., Belamri, T., 2006. Comparison of computational results obtained from a Homogeneous cavitation model with experimental investigations of three inducers. J. Fluid Eng. 128 (6), 1308–1323. https://doi.org/10.1115/1.2353265, 10.1115/1.2353265.
Mousmoulis, G., Karlsen-Davies, N., Aggidis, G., Anagnostopoulos, I., Papantonis, D., 2019. Experimental analysis of cavitation in a centrifugal pump using acoustic emission, vibration measurements and flow visualization. Eur. J. Mech. - B/Fluids 75, 300–311. https://doi.org/10.1016/J.EUROMECHFLU.2018.10.015.
Okita, K., Matsumoto, Y., Kamijo, K., 2003. Numerical analysis for unsteady cavitating flow in a pump inducer. Paper Presented at the Fifth International Symposium on Cavitation (CAV2003). Cav03-OS-4-12, Osaka, Japan.
Okita, K., Ugajin, H., Matsumoto, Y., 2009. Numerical analysis of the influence of the tip clearance flows on the unsteady cavitating flows in a three-dimensional inducer. Journal of Hydrodynamics, Ser. B 21 (1), 34–40.
Pace, G., Valentini, D., Pasini, A., Torre, L., Fu, Y., d'Agostino, L., 2015. Geometry effects on flow instabilities of different three-bladed inducers. J. Fluid Eng. 137 (4) https://doi.org/10.1115/1.4029113, 10.1115/1.4029113.
Pace, G., Valentini, D., Pasini, A., Torre, L., Hadavandi, R., d'Agostino, L., 2017. Inducer and centrifugal pump contributions to the rotordynamic fluid forces acting on a space turbopump. J. Fluid Eng. 140 (2) https://doi.org/10.1115/1.4037977, 10.1115/1.4037977.
Plesset, M.S., 2021. The dynamics of cavitation bubbles. J. Appl. Mech. 16 (3), 277–282. https://doi.org/10.1115/1.4009975, 10.1115/1.4009975.
Rakibuzzaman, M., Kim, K., Suh, S.-H., 2018. Numerical and experimental investigation of cavitation flows in a multistage centrifugal pump. J. Mech. Sci. Technol. 32 (3), 1071–1078. https://doi.org/10.1007/s12206-018-0209-6, 10.1007/s12206-018-0209-6.
Rayleigh, L., 1917. VIII. On the pressure developed in a liquid during the collapse of a spherical cavity. London, Edinburgh Dublin Phil. Mag. J. Sci. 34 (200), 94–98. https://doi.org/10.1080/14786440808635681, 10.1080/14786440808635681.
Shojaeefard, M.H., Hosseini, S.E., Zare, J., 2019. CFD simulation and Pareto-based multi-objective shape optimization of the centrifugal pump inducer applying GMDH neural network, modified NSGA-II, and TOPSIS. Struct. Multidiscip. Optim. 60 (4), 1509–1525. https://doi.org/10.1007/s00158-019-02280-0, 10.1007/s00158-019-02280-0.
Stripling, L., Acosta, A., 1962. Cavitation in Turbopumps—Part 1.
Svennberg, U., Asnaghi, A., Gustafsson, R., Bensow, R.E., 2020. Experimental analysis of tip vortex cavitation mitigation by controlled surface roughness. J. Hydrodyn. 32 (6), 1059–1070. https://doi.org/10.1007/s42241-020-0073-6, 10.1007/s42241-020-0073-6.
Torre, L., Pasini, A., Cervone, A., d'Agostino, L., 2009. Experimental performance of a tapered axial inducer: comparison with analytical predictions. In: 45th AIAA/ASME/SAE/ASEE Joint Propulsion Conference & Exhibit.
Wang, L., Chang, J., 2010. Computational theory of cavitating flows for hydraulic turbomachinery with consideration of influence of water quality. Sci. China Technol. Sci. 53 (12), 3341–3348. https://doi.org/10.1007/s11431-010-4149-3, 10.1007/s11431-010-4149-3.
Wang, K., Luo, G., Li, Y., Xia, R., Liu, H., 2020. Multi-condition optimization and experimental verification of impeller for a marine centrifugal pump. Int. J. Nav. Archit. Ocean Eng. 12, 71–84. https://doi.org/10.1016/J.IJNAOE.2019.07.002.
Wang, J., Sun, L., Zhou, Y., Liu, Y., Zhao, F., 2023. Numerical simulation of cavitation characteristics of a centrifugal pump based on an improved ZGB model. Process. 11, 2023 https://doi.org/10.3390/PR11020438. Page 438 11, 438.
Xu, Y., Tan, L., Liu, Y., Cao, S., 2017. Pressure fluctuation and flow pattern of a mixed-flow pump with different blade tip clearances under cavitation condition. Adv. Mech. Eng. 9 (4), 1687814017696227. https://journals.sagepub.com/doi/abs/10.1177/1687814017696227, 10.1177/1687814017696227.
Zare, J., Hosseini, S.E., Rastan, M.R., 2024. Airborne dust-induced performance degradation in NREL phase VI wind turbine: a numerical study. Int. J. Green Energy 21, 1295–1314. https://doi.org/10.1080/15435075.2023.2246544.
Zhang, J.-y., Du, Y.-x., Liu, J.-q., Sun, Y.-r., Yao, Z.-f., Zhong, Q., 2022. Experimental and numerical investigations of the collapse of a laser-induced cavitation bubble near a solid wall. J. Hydrodyn. 34 (2), 189–199. https://doi.org/10.1007/s42241-022-0017-4, 10.1007/s42241-022-0017-4.
Zhao, X.a., Huang, B., Chen, T., Wang, G., Gao, D., Zhao, J., 2017. Numerical simulations and surrogate-based optimization of cavitation performance for an aviation fuel pump. J. Mech. Sci. Technol. 31 (2), 705–716. https://doi.org/10.1007/s12206-017-0122-4, 10.1007/s12206-017-0122-4.